frontiers | Frontiers in Energy Research

TYPE Original Research
PUBLISHED 09 February 2026
DOI 10.3389/fenrg.2025.1726701

OPEN ACCESS

EDITED BY
Li Sun,
Southeast University, China

REVIEWED BY
Marcin Sosnowski,
Jan Długosz University, Poland
Xiaojing Han,
Shanxi Vocational University of Engineering Science and Technology, China
Fatemeh Isania,
University of Padua, Italy

*CORRESPONDENCE
Elham Abohamzeh,
elham.abohamzeh@aut.uni-saarland.de

RECEIVED 16 October 2025
REVISED 04 December 2025
ACCEPTED 15 December 2025
PUBLISHED 09 February 2026

CITATION
Abohamzeh E, Theis D and Frey G (2026) Exploring the potential of a novel segmented concept of real-scale open sorption storage via CFD modeling and performance evaluation.
Front. Energy Res. 13:1726701.
doi: 10.3389/fenrg.2025.1726701

Exploring the potential of a novel segmented concept of real-scale open sorption storage via CFD modeling and performance evaluation

Elham Abohamzeh[1]*, Danjana Theis[2] and Georg Frey[1]

[1]Automation and Energy Systems, Saarland University, Saarbrücken, Germany, [2]Hochschule für Technik und Wirtschaft Saarland, University of Applied Sciences, Saarbrücken, Germany

Sorption heat storage enables high-density, low-loss thermal energy storage from summer to winter through reversible adsorption–desorption, offering strong potential for both short-term and seasonal solar heating in residential applications. In this work, a novel segmented reactor concept is developed for an open sorption heat storage system, enabling flexible configuration and scalable capacity. A numerical simulation is developed and the performance of the designed module containing zeolite 13XBF is comprehensively evaluated with simulations under various operating conditions and performance indicators. Numerical results indicate an energy density of approximately 115.6–144 kWh/m^3, depending on the boundary conditions for the proposed reactor, mostly affected by the relative humidity of incoming air. Furthermore, the segmented design yields exceptionally low pressure drops in the bed, ranging from 71 Pa to 203 Pa for mass flow rates between 50 kg/h and 120 kg/h, thereby reducing fan power requirements. Detailed simulations reveal that increasing the relative humidity of the incoming airflow and reducing the initial and inlet temperature under constant partial pressure contribute to higher output temperature, power, and energy density. Raising the inlet vapor pressure from 5 mbar to 25 mbar increased the useful energy from 23.9 MJ to 29.8 MJ, and energy density from 115.6 kWh/m^3 to 143.3 kWh/m^3. Increasing the airflow rate raises the instantaneous output power. However, it may also shift the outlet temperature outside the desired range for residential space heating, which highlights the importance of careful control and optimization. A CFD-based design study shows that the initial segmented reactor uses the two beds unevenly and yields imbalanced outlet temperatures, while simple geometric changes—shortening the upper bed and adding an inlet diffuser—make the flow and temperature fields more uniform, extend the high-temperature discharge period by about 22%, and increase the volumetric energy density.

KEYWORDS

adsorption, energy density, modular design, numerical simulation, open sorption heat storage system

1 Introduction

The rising energy demand in the building sector coupled with the urgent need to reduce dependence on fossil fuels, has made the development of thermal energy storage systems a critical priority in energy engineering. Among them, thermochemical energy storage (TCES) has gained significant attention due to its high energy density and potential for long-term storage with minimal thermal losses. There is considerable technical potential in the development of compact and efficient long-duration storage systems. These systems use storage materials, such as sorption materials or hygroscopic salts, to store heat energy. In contrast to storing sensible heat (for example, in water tanks), the heat in such materials is stored chemically or physically through binding mechanisms, rather than just through temperature changes. This results in energy storage densities, which are often 6 to 7 times higher than that of water-based systems (Kerskes et al., 2012). Sorption-based heat storage systems, as a subcategory of TCES systems, are based on the reversible sorption process between a sorbent and a sorbate. During the charging phase, typically occurring in summer, thermal energy at elevated temperatures is supplied to drive the desorption process. This heat input removes the sorbate from the saturated sorbent, causing it to evaporate and exit the reactor in gaseous form. In the discharging phase, moist air containing water vapor enters the reactor. As the vapor interacts with the regenerated (unsaturated) sorbent, adsorption occurs, releasing the associated enthalpy of adsorption. This released thermal energy can then be utilized for heating purposes.

Several previous studies have demonstrated the high potential of TCES systems. Schmidt and Linder (Schmidt and Linder, 2020) presented a novel seasonal TCES concept for residential buildings using the reversible $Ca(OH)_2/CaO + H_2O$ reaction, where surplus renewable electricity drives dehydration in summer and liquid water enables efficient exothermal discharge in winter. The system design includes a mechanically assisted fluidized-bed reactor and integrates waste heat from charging for domestic hot water, achieving a theoretical storage efficiency of up to 96% and an energy density of 132–215 kWh/m^3. With low-cost, abundant materials and loss-free long-term storage, the concept shows strong potential to balance renewable electricity supply with winter heat demand, though practical performance still depends on reactor validation, heat exchanger efficiency, and long-term cycling tests. Fasano et al. (2019) experimentally investigated 13X zeolite with liquid sorbates (water, ethanol, and a water–ethanol mixture) as a simplified approach to long-term thermal energy storage at ambient pressure. While liquid hydration yielded lower storage densities than conventional vapor-based systems, the results (49–80 kWh/m^3) were still comparable to latent heat storage, with the ethanol–water mixture offering the best trade-off between energy density, regeneration temperature, and cycling stability. The study highlighted practical advantages such as simplicity, robustness, and low cost, and illustrated a potential application in improving cold-start performance of diesel standby generators, though challenges remain with sorbent degradation and reduced efficiency compared to vapor sorption systems. Hassanabadi et al. (2025) have suggested a lightweight shell-and-tube sorption reactor that substitutes a thin carbon-steel shell for the typical heavy vacuum chamber to reduce mass and complexity while preserving vacuum integrity, disk-shaped $CaCl_2$–silica gel composites (with PVA binder and expanded natural graphite for improved heat diffusion) are placed inside stainless-steel tubes, and the heat transfer fluid flows on the shell side, allowing for compact, modular scaling. The prototype demonstrated specific energy of 0.74 MJ/kg and specific power of 267 W/kg.

Although sorption materials exhibit a high theoretical energy density, this potential is not fully realized in practical sorption heat storage systems (Palacios et al., 2022). Consequently, system design plays a crucial role in bridging this gap. Comprehensive evaluations have demonstrated that reactor design is pivotal for effective energy transfer and directly influences both the capacity and efficiency of the system. An optimal reactor design must ensure efficient heat and mass transfer to minimize thermal and pressure losses. Furthermore, achieving high energy storage density requires compact reactor configuration. One of the main tools for designing and optimizing sorption heat storage systems is mathematical modeling, which, if used properly, can reduce cost and save time. This approach allows for the design of the storage system to be optimized and its performance to be analyzed without the need for costly experiments (Krese et al., 2018). Moreover, numerical modelling plays a critical role in improving system design and performance to achieve maximum energy storage and efficiency, developing strategies to regulate system operations (e.g., charging and discharging processes) under different conditions, and energy efficiency assessment. Kuznik et al. (2019) developed a numerical model based on experimental data to investigate the performance of a full-scale zeolite 13X open heat storage system designed for integration into building ventilation systems. They have investigated the influence of desorption temperature, airflow rates, relative humidity, and bed thickness. They have found around 70% efficiency for the discharging process and an overall efficiency of 36%. Mette et al. (2014a) conducted simulations to investigate two reactor designs for sorption heat storage with zeolite 13XBFK: an integrated and an external reactor. They developed numerical models and validated the models by experimental testing. The integrated reactor is directly incorporated into the material storage reservoir, whereas the external reactor is designed to be separated from the material storage reservoir. Therefore, there is a need for transporting material between the reservoir and the reactor. This design leads to minimizing heat losses and heat capacity, especially during the charging phase. Based on numerical simulation, a maximum temperature of 56 °C, indicating a temperature increase of 26 K, is predicted in the fixed bed for integrated design, corresponding to a thermal power output of 1.46 kW. For the external reactor, the numerical simulation predicted a temperature increase of approximately 26 K in the airflow, corresponding to a thermal power of 860 W. Reichl et al. (2016) utilized CFD simulations to model an open sorption heat storage drum reactor and validated the model with experiments. They used two different approaches for the simulation of the movement and behavior of particles in the rotating drum. Their observations showed that more accurate results can be achieved with the discrete particle method; however, this method is computationally expensive and time-consuming for complex geometries. The porous volume approach was more efficient but required the development of a mixing algorithm to simulate the movement of particles within the bed. They also observed enhanced airflow distribution and sorption efficiency within the drum reactor by addressing mixing, dead

zones, and unused areas in the reactor. A quasi-continuous crossflow reactor was developed by Kerskes et al. (2011) for low-temperature heat storage applications, particularly for building heating with solar energy. The authors conducted numerical modeling to gain a deep understanding of heat and mass transfer in the reactor. The simulation results have been validated with experimental data from a lab-scale reactor. The numerical simulations were used for optimizing the reactor design and evaluating different reaction strategies. Jänchen et al. (2015) developed a simplified model of CFD simulation on a sorption reactor including Linde-type 4A-zeolite beads and honeycomb structures (with and without binder) to investigate the differences in the adsorption dynamics of these two types. They also conducted experiments on a 1.5 L lab-storage reactor and compared the results from the model and experiments. Based on their observation, the simplified model was helpful in the visualization of airflow patterns but could not provide an accurate prediction of dynamic adsorption behavior. The adsorption dynamics of the binder-less zeolite honeycombs were much better compared to the beads in experiments, but similar adsorption performance was observed in simulations. Padamurthy et al. (2022) investigated a lab-scale open zeolite–water sorption heat storage prototype designed for low-temperature charging of about 95 °C. Using 2.8 kg of zeolite 13X and 4A pellets in a cylindrical fixed bed with multiple sieves, they ran 15 sequential charge–discharge cycles and measured temperatures, relative humidity (RH), pressure, mass change and airflow to characterize performance and stability. For zeolite 13X, they report average volumetric energy storage densities in the range of 57–129 kWh/m^3; zeolite 4A performs significantly worse on all metrics. A temperature lift of roughly 30 K above room temperature is maintained for about 6 h after only 3 h of charging. Overall, the study demonstrates the technical feasibility of open zeolite sorption storage at relatively low charging temperatures and provides experimental benchmarks for energy density, efficiency and pressure drop relevant to building-scale space and water heating. Strong et al. (2022) experimentally investigated an open silica gel/water vapor adsorption thermal energy storage system and systematically optimize its operating conditions. Using a 62.8 cm^3 packed column (about 50 g silica gel), they varied inlet RH, particle size, regeneration temperature, insulation level and air flow rate, and evaluate their impact on energy storage density (ESD), temperature lift, saturation/breakthrough times, thermal power and pressure drop. They found that higher inlet RH and regeneration temperature (up to about 120 °C) significantly increase energy density and maximum temperature lift, while insulation around column and piping raises ESD by ~17% by reducing heat losses. Flow rate strongly controls thermal power and saturation time, while particle size mainly affects pressure drop and, to a lesser extent, saturation time. Under optimized conditions (RH = 90%, 12–20 mesh, 120 °C regeneration, and additional insulation), the system reaches an energy storage density of about 200.7 kWh/m^3, a maximum temperature lift of 28.5 °C, and average thermal power of 5.9 W.

Numerical modelling and simulation play a crucial role in the development of sorption heat storage systems before any hardware is built. A numerical model makes it possible to explore a wide design space (geometry, materials, operating conditions) at much lower cost. In this context, several numerical studies have been conducted to analyze and optimize sorption storage systems, for example to assess the influence of operating conditions and reactor design on energy density and power, and compare different working pairs or reactor concepts. These modelling works provide important insight into the dominant transport and reaction mechanisms and help to pre-select promising designs before building and testing full-scale prototypes. Abohamzeh and Frey (2022) developed a 1D numerical model of the adsorption process in a fixed-bed zeolite 13X/water reactor and used it to explore how operating conditions affect storage performance. The authors performed a parametric study varying key boundary conditions and show that higher desorption temperatures and higher inlet vapor pressures significantly increase the mean adsorption enthalpy, outlet air temperature, and total adsorbed water, thus boosting the useful storage capacity, but also tend to shorten the discharge duration because the reaction front moves faster through the bed. The air mass flow rate mainly affects the length of the discharge: increasing flow shortens the discharge time and raises instantaneous power, while having comparatively little influence on peak outlet temperature within the investigated range. The authors also computed indicative storage densities and specific powers and provided polynomial correlations (response-surface fits) that relate mean adsorption enthalpy, discharge time, and adsorbed water to the three operating parameters, offering simple engineering formulas for preliminary design and performance estimation of zeolite-based seasonal heat storage. Abohamzeh et al. (2024) developed a transient axisymmetric numerical model of a closed zeolite-13X/water sorption heat storage bed equipped with straight and Y-shaped fins to address the inherently low thermal conductivity of the adsorbent bed. By coupling detailed heat and mass transfer with sorption models and applying response surface methodology, they systematically optimized fin length and branch angle to maximize the outlet heat transfer fluid temperature and power output. The optimized Y-shaped fin configuration substantially improved reactor performance compared with straight fins and the finless case. It increased the average outlet temperature by up to 8.7 K and raised the average output power by 103% and 238.8% relative to the straight-fin and finless configurations, respectively. Hu et al. (2022) developed a spatially resolved 2D model of a zeolite–water packed-bed sorption heat storage reactor, including detailed adsorption kinetics and local heat and mass transfer. Using this model, the authors analyze how radial porosity oscillations and wall effects shape local velocity, temperature and loading fields inside the zeolite bed. A parametric study shows how particle size, bed height, diameter ratio and superficial velocity influence outlet temperature, storage density and pressure drop, highlighting trade-offs between high sorption energy density and acceptable hydraulic losses. The study shows that smaller particles and lower bed heights increase storage density but shorten discharge time and can worsen the balance between energy and pressure drop. Increasing superficial velocity further boosts energy density (up to roughly 245 kWh/m^3) but also leads to higher pressure losses, highlighting a clear trade-off between thermal performance and hydraulic effort.

In the context of reactor design, a modular reactor design offers significant advantages. Non-modular systems often lack flexibility, making it difficult to scale and adapt to different environments. Additionally, non-modular configurations provide limited control over localized heat transfer processes, often resulting in higher energy consumption, inconsistent performance,

and high pressure drops in open sorption systems. Modular designs enable easier integration, targeted improvements, and more manageable simulation and validation processes, ultimately accelerating innovation and system optimization.

In this work, a realistic-scale, modular, open sorption heat storage system was designed, and its performance was evaluated through detailed CFD simulations. Following validation of the developed CFD model, a series of simulations were conducted to assess the prototype's performance under realistic boundary conditions. The model was further applied to analyze the energy conversion chain of the zeolite-based heat storage system. The impact of varying boundary conditions on system behavior was systematically investigated, leading to targeted design modifications aimed at enhancing overall efficiency. These improvements resulted in a more uniform outlet temperature profile and improved operational performance. Section 2 describes the open, atmospheric-pressure sorption heat-storage concept: solar-driven desorption during charging, and adsorption-based heat release during discharging. The reactor is designed as a modular and segmented system to ensure efficient coupled heat–mass transfer.

2 The proposed open sorption reactor concept

The focus of this work is an open sorption heat storage system operating under atmospheric pressure. In this configuration, the sorbate is brought into direct contact with the sorbent bed via controlled airflow. During the charging phase (typically in summer), thermal energy harvested from solar collectors is supplied to the reactor, driving the desorption of water vapor from the sorbent material. In the discharging phase (typically in winter), the moist air is reintroduced into the reactor, where it is adsorbed by the sorbent, releasing thermal energy that can be utilized for space heating (Kwasi-Effah and Okpako, 2025).

The core component of a thermochemical energy storage system is the reactor, where thermal charging and discharging processes take place. In addition to heat transfer, the reactor also facilitates the chemical and physical mechanisms associated with mass transfer. Consequently, the reactor must be engineered to ensure efficient transport of both heat and mass. Key design objectives focus on achieving a high temperature increase within the reactor to deliver the necessary thermal output during the discharging phase, while also ensuring that the storage material is fully charged and regenerated during both the charging and discharging cycles for optimal system performance.

Various open sorption reactor concepts have already been proposed, including segmented plate-type stores integrated into rectangular boxes, unsegmented cylindrical fixed beds, and moving-bed systems with external silos (Weber et al., 2016; Kuznik et al., 2019; Kerskes et al., 2012). These designs differ in geometry, flow pattern and degree of internal controllability. The design studied in this work is a repeatable vertical cylindrical fixed-bed module with a segmented internal layout, consisting of radial segment pairs, supplied by a central axial inlet and operated via rotary valves at the segment outlets. This configuration enables staged use of individual segments and benefits from the more uniform flow distribution provided by the cylindrical geometry. The main geometric and operational differences between representative previous reactors and the proposed segmented cylindrical module are summarized in Table 1.

The sorption heat storage system developed in this work uses the segmented cylindrical reactor as a modular building block. As shown in Figure 1a, this design approach enables the reactor to be assembled from multiple standardized modules, which can be configured in parallel or series depending on the required capacity and application. Such modularity not only facilitates system expansion and prototyping but also simplifies maintenance, upgrades, and experimental adjustments without necessitating a complete redesign.

Within each module, controllable inlet valves distribute the air or water vapor between the bed segments. This segmentation allows sequential charging and discharging for example, segments one and 2 can be activated first, followed by segments 3 and 4. The same principle can be applied during discharge to realize stepwise heat release according to the thermal demand. This local flow control (i) improves thermal efficiency by avoiding unnecessary use of the full bed volume, (ii) enables more accurate process monitoring and optimization, and (iii) supports intelligent energy management tailored to real-time heating requirements.

In summary, the modular reactor design not only enhances simulation and fabrication efficiency but also paves the way for scalable, robust, and adaptable thermal storage solutions suitable for both laboratory investigations and real-world building applications. In numerical study, the simulation focuses on a single representative module, presented in Figure 1b, serving as a fundamental building block of the overall multi-stage reactor. Each module is internally segmented, allowing for detailed control and localized analysis of heat and mass transfer processes.

3 Describing the numerical procedure

3.1 Physical model

Figure 2 illustrates the modular open sorption heat-storage reactor, including the airflow path, showing distribution and movement through the zeolite-packed bed, and the dimensional parameters that define the reactor geometry, such as inlet and outlet pipe diameters, reactor height, cone angles, and the curvature radius of the lower section. These parameters are used in both the reactor design process and the CFD model development.

Geometrical parameters of the module, thermophysical properties of zeolite, water vapor, metal and other operating parameters of the adsorption system considered in the present study are listed in Table 2.

3.2 Governing equations

3.2.1 Adsorption model

The adsorbed amount onto the surface of an adsorbent can be describe as a function of the partial pressure of adsorbate and the temperature of the adsorbent. In this work, the Dubinin–Astakhov (D–A) micropore filling model is used for the calculation of the equilibrium loading (Bering et al., 1966). It is a semi-empirical

TABLE 1 Comparison of the proposed segmented cylindrical reactor module with previous open sorption reactor designs.

Feature	Proposed segmented cylindrical module	SolSpaces project (Weber et al., 2016)	Full-scale open reactor (Kuznik et al., 2019)	CWS-NT reactor (ITW) (Kerskes et al., 2012)
Basic shape/unit	Vertical cylindrical module: Multiple identical modules form the store	Single rectangular store integrated in the building (technical room)	Two separate cylindrical reactors (each one packed bed)	Central rectangular reactor with external sorbent silos in a single integrated plant
Store type	Combined reactor and storage	Combined reactor and storage	Combined reactor and storage	Moving bed with sorbent circulation between reactor and silos; storage mainly in silo
Internal structure of bed	Cylinder contains two packed-bed segments (upper/lower), each split into radial segment pairs (ring-shaped sectors)	The box is divided into four quadrants, each subdivided into six horizontal segments, resulting in 24 flat rectangular segments	In each cylinder the bed is one unsegmented packed-bed layer (no sectors)	Reactor with moving packed bed; no fixed internal segments
Flow pattern in bed	Air flows axially in central pipe, then radially outwards through chosen segment pair	Air enters the central duct and flows through the selected segment pair to the outlet channels at the outer edges	Vertical flows through entire bed (axial up/down)	Crossflow of air through a gravity-driven moving bed
Segmentation inside bed	Segmentation into packed-bed segments (upper/lower) and radial segments; each segment pair represents a distinct reactor sub-volume	Segmentation as quadrants × levels; segment pairs chosen at the outlet	No internal segmentation: only whole reactors can be switched	No fixed segments
Internal control elements	Rotary valves at each segment outlet, enabling selective charging and discharging segment pairs	Sliding gates at outlet channels to choose plate pairs; whole box is one unit	Control only at reactor level with choosing reactor, mass flow, T, RH); no internal valves	Control via material mass flow, air valves, fans, hydraulics
Flow distribution/symmetry	Cylindrical symmetry with central inlet resulting in more uniform flow distribution to different segments	Rectangular geometry; air enters the central inlet channel and exits via four outlet channels at the vertical edges; segment selection by a sliding-gate mechanism	Simple cylinder with one unsegmented packed bed; vertical through-flow	Rectangular cross-section; air enters laterally via flow funnels, ensuring uniform flow over the reactor cross-section
Scalability concept	Standardized modular storage unit; total capacity is adjusted by the number of identical cylindrical modules	The rectangular store should be sized (volume, number of levels) to match the building heat demand	The prototype consists of two separate reactors that can be connected in series or in parallel; scale-up beyond this prototype is not discussed	Good scalability due to material transport (decouples storage capacity and reactor power); requires separate material storage and transport

isothermal model based on Polanyi's potential theory, where the assumption is that the adsorbent's pore distribution corresponds to the Gaussian energy distribution. Based on this theory, adsorption is controlled by micropore volume rather than surface area, for pores smaller than 2 nm. The pore-filling degree, φ, is defined as the adsorbed volume divided by the maximum adsorption volume, as given in Equation 1 (Do, 1998; Bering et al., 1966):

$$\varphi = \frac{W^*}{W_{0,DA}} \tag{1}$$

A is the adsorption potential and is defined as the work needed to move an adsorbate from its equilibrium pressure in the gas phase to its saturated vapor pressure where it is adsorbed, and can be calculated with Equation 2 (Bering et al., 1966; Do, 1998):

$$A = R_w T ln\left(\frac{p_s}{p_w}\right) \tag{2}$$

Here, p_w is the equilibrium pressure of the adsorbate, p_s is the saturation vapor pressure of the adsorbate at the temperature T, and R_w is the specific gas constant of the adsorbate.

The uptake based on the volume of the sorbate is defined as presented in Equation 3 (Do, 1998):

$$W^* = W_{0,DA}\, exp\left[-(A/E_{DA})^n\right] \tag{3}$$

Where $W_{0,DA}$ is the maximum volumetric sorbate adsorption loading, n is a constant related to the percent of pore filling and represents the heterogeneity parameter describing the micropore-size distribution, E_{DA} is the characteristic energy, which is the characteristic energy that reflects the strength of the adsorbate–adsorbent interactions. Here, three parameters ($W_{0,DA}$, n, and E_{DA}) need to be identified.

The mass-related loading, X^* is defined based on the volumetric loading and using the density of the adsorbed phase, $\rho(T)$

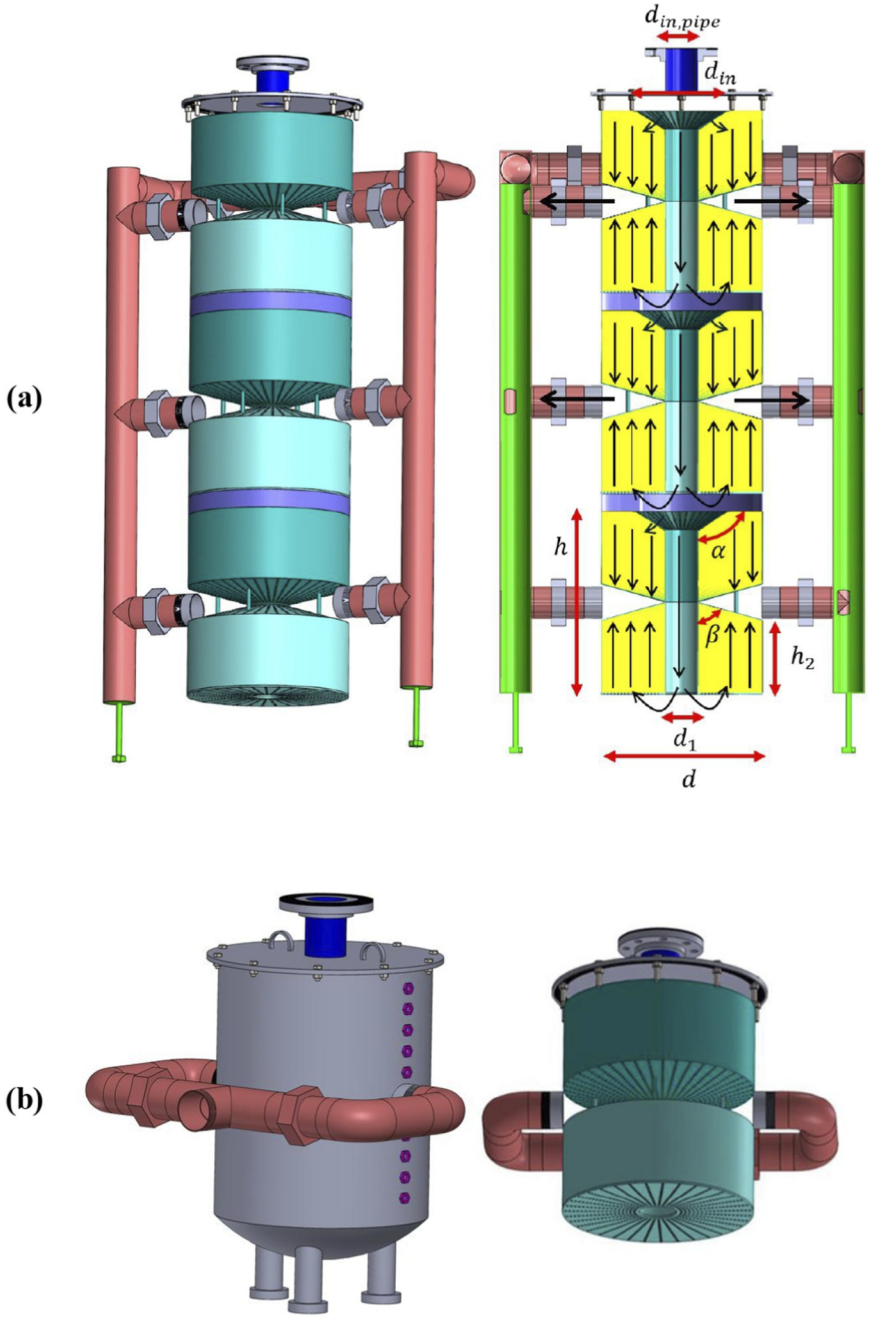

FIGURE 1
(a) Schematic of the zeolite sorption reactor with modular container and piping arrangement, **(b)** Single representative module investigated in numerical simulation (Farisy, 2022).

(Equations 13, 14):

$$X^* = \rho(T) W^* \tag{4}$$

The density of adsorbed water can be expressed as a function of temperature (Equations 13, 14):

$$\rho(T) = \frac{\rho_{20\,^\circ C}}{1 + \beta_{20\,^\circ C}(T - 293.15)} \tag{5}$$

Where $\boldsymbol{\rho_{20\,^\circ C}}$ is the density and $\boldsymbol{\beta_{20\,^\circ C}}$ is the thermal expansion coefficient of adsorbate at 20 °C. From Equations 4, 5, the following relationship for the equilibrium loading can be specified, as given in Equation 6 (Bering et al., 1966; Do, 1998):

$$X^* = \rho(T) W_{0,DA}\, exp\,[-(A/E)^n] \tag{6}$$

3.2.2 Kinetics model

There are three main steps in the adsorption process:

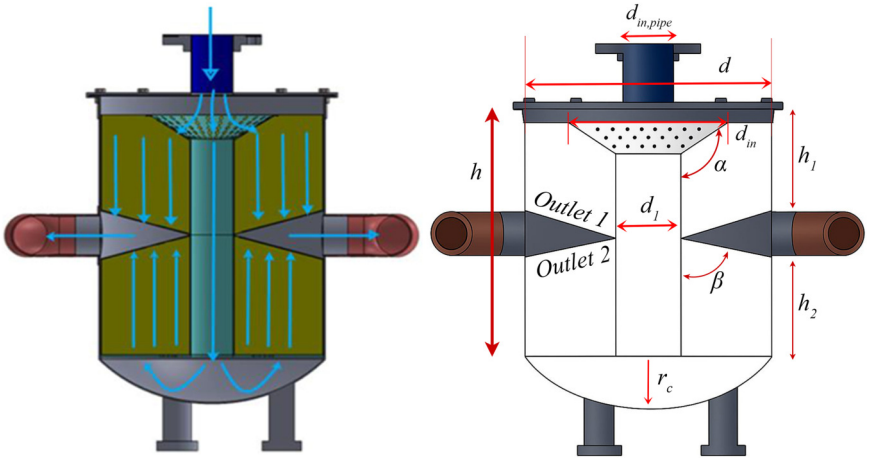

FIGURE 2
Flow path (left) and dimensional parameters of the sorption heat storage reactor (right) (Farisy, 2022).

1. External mass transfer, or the transport of the adsorbate from the fluid phase to the particle surface via the concentration boundary layer.
2. Internal Mass Transfer or diffusion of the adsorbate through the pore system inside the particle.
3. Adsorption at the internal adsorption surface (Mersmann and Kind, 1980).

The release of the adsorbate from the adsorbent surface initiates desorption, which proceeds in the opposite direction.

Generally, there are three main approaches for the evaluation of the adsorption kinetics: the equilibrium model (Duquesne et al., 2014), the diffusion model, and the linear driving force (*LDF*) model (Lagergren, 1898). Adsorption kinetics are frequently overestimated by equilibrium models, *LDF* models typically underestimate them over short time frames but yield consistent results over longer ones (Qiu et al., 2009; Sircar and Hufton, 2000). The *LDF* model, originally introduced by Glueckauf (1955), simplifies the three-step process by assuming a homogeneous adsorption loading over the particle radius.

An effective diffusion coefficient, δ_{eff}, which accounts for the resistance of the concentration boundary layer, is used to characterize the total mass transfer resistance. The concentration difference between the equilibrium loading X^* and the current loading X is the driving factor for the temporal variation in the average adsorbent loading (Glueckauf, 1955), as given in Equation 7:

$$\frac{\partial X}{\partial t} = 15\delta_{eff}\left(\frac{1}{0.5d_p^2}\right)\left[X^*(T,p_w) - X\right] \tag{7}$$

The *LDF* approach is frequently used to describe adsorption processes since it is simpler than more detailed particle models. According to studies it is in good agreement with experiments (Kast, 1988).

The surface adsorption (Step 3) together with internal (Step 2) and external (Step 1) mass-transfer resistances are incorporated via the effective diffusivity δ_{eff}. In most cases, the rate is governed by the intraparticle (internal) resistance (Kast, 1988).

In these equations, X is the adsorbate loading, and X^* is the equilibrium loading, the mass of adsorbate per mass of dry sorbent at equilibrium. d_p is the average diameter of the zeolite beads and δ_{eff} is the effective diffusion coefficient, which can be calculated based on Equations 8, 9 (Bathen and Bäth, 2001):

$$\delta_{eff} = \frac{D_{ges}/\mu}{1+\alpha(x)} \tag{8}$$

$$\alpha(x) = \frac{\rho_s RT}{\varepsilon_p M_{ads}}\frac{\partial X^*}{\partial p_w} \tag{9}$$

Here, μ denotes the tortuosity factor, M_{ads} the molar mass of water, ε_p the intraparticle porosity of the zeolite, and $\frac{\partial X^*}{\partial p_w}$ the isotherm slope.

The overall diffusion resistance D_{ges} is give by Equation 10 (Bathen and Bäth, 2001):

$$D_{ges} = \left[1/D_{Kn} + 1/D_{i,j}\right]^{-1} \tag{10}$$

D_{Kn} represents the resistance due to Knudsen diffusion, while $D_{i,j}$ is the resistance associated with binary free-gas diffusion of components i and j. The expressions for D_{Kn} and $D_{i,j}$ are provided in Equations 11, 12 (Kast, 1988):

$$D_{kn} = \frac{4}{3}d_m\sqrt{\frac{RT}{2\pi M_{ads}}} \tag{11}$$

$$D_{i,j} = \frac{1.013T^{1.75}10^{-7}\left[\frac{1}{M_i}+\frac{1}{M_j}\right]^{1/2}}{p\left[\left(\sum v_i\right)^{1/3}+\left(\sum v_j\right)^{1/3}\right]^2} \tag{12}$$

Here, M_i and M_j denote the molar masses in *kg/kmol*, while $\sum v_i$ and $\sum v_j$ correspond to the diffusion volumes of the respective molecules.

3.2.3 Adsorption enthalpy

The adsorption enthalpy is obtained by adding the vaporization enthalpy $\Delta \boldsymbol{H}_v$, and the binding enthalpy. The adsorption enthalpy of

10.3389/fenrg.2025.1726701

TABLE 2 Geometrical and thermophysical parameters.

Parameter	Value	Unit	Description
$c_{p,a}$	1,005	J/(kg K)	Specific heat capacity of dry air
$c_{p,s}$	475	J/(kg K)	Specific heat of steel
$c_{p,z}$	880	J/(kg K)	Specific heat capacity of zeolite-13XBF
d_1	90	mm	Diameter of the air channel
d	446	mm	Total diameter of the reactor
d_{in}	267	mm	Inlet diameter reactor
$d_{in,pipe}$	89	mm	Inlet diameter pipe
d_m	300	nm	Macropore diameter
d_p	2	mm	Average diameter of zeolite particles
E_{DA}	1,192.25	kJ/kg	Characteristic energy
h_1	200	mm	Height of the upper segment
h_2	200	mm	Height of the lower segment
h	500	mm	Total length of the reactor
k_{ss}	44.5	W/(m K)	Thermal conductivity of stainless steel
λ_s	0.4	W/(m K)	Thermal conductivity of zeolite-13XBF
M_a	28.97	g/mol	Air molar mass
M_w	18.02	g/mol	Water vapor molar mass
n	1.55	-	Exponent in the dubinin equation
r_c	10	mm	Curvature height
R	8.314	J/(mol K)	Ideal gas constant
R_a	287	J/(kg K)	Specific gas constant of dry air
t	2	mm	Wall and channel thickness
$W_{0,DA}$	314.03	mL/kg	Maximum adsorption volume
α	122	Deg	Angle of the bed inlet
β	75	Deg	Angle of the bed outlet
ε_b	0.4	-	Porosity of the desorption bed
ε_p	0.6	-	Porosity of zeolite particle
η	1.8×10^{-5}	Pa s	Dynamic viscosity of air
ρ_s	7,850	kg/m^3	Density of stainless steel
ρ_z	1,150	kg/m^3	Particle density
$\rho_{z,b}$	700	kg/m^3	Bulk density of zeolite
μ	4	-	Tortuosity

(Continued on the following page)

zeolite, $\Delta \boldsymbol{H}$, as a function of the adsorption volume uptake, is given by Equation 13 (Mette, 2014b):

$$-\Delta H_{ads} = \Delta H_v + E\left(ln\frac{W_{0,DA}}{W^*}\right)^{1/n} + \frac{E\beta T}{n}\left(ln\frac{W_{0,DA}}{W^*}\right)^{-(n-1)/n} \quad (13)$$

3.2.4 Mass and energy balance equations

The movement of water vapor inside the reactor involves multiple mechanisms: axial dispersion; transport due to the flow of moist air, and the partial uptake of water vapor by the sorbent materials. Therefore, the changes in water vapor concentration can be expressed as in Equation 14 (Mette et al., 2014a):

$$\varepsilon_b \frac{\partial w}{\partial t} = \frac{\partial}{\partial z}\left(D_{ax}\frac{\partial w}{\partial z}\right) + \frac{1}{r}\frac{\partial}{\partial r}\left(D_r r\frac{\partial w}{\partial r}\right) - v\frac{\partial w}{\partial z} + (1-\varepsilon_b)\frac{\rho_z}{\rho_a}\frac{\partial X}{\partial t} \quad (14)$$

Here, $\boldsymbol{D_{ax}}$ and $\boldsymbol{D_r}$ denote the effective axial and radial dispersion coefficients. w represents the water vapor content in the air, $\boldsymbol{\varepsilon_b}$ is the bed porosity, and $\boldsymbol{\rho_a}$ and $\boldsymbol{\rho_z}$ are the densities of the fluid and the zeolite bed, respectively.

To account for both diffusion and convection effects, the heat transfer within the reactor can be modeled using the following equation assuming a constant fluid density. The energy equation also includes a source term to represent the heat generated or absorbed during the charging or discharging processes (Mette, 2014b).

$$\begin{aligned}\left[\varepsilon_b\rho_a c_{p,a} + \rho_{p,z}(1-\varepsilon_b)\left(c_{p,z} + Xc_{p,ads}\right)\right]\frac{\partial T}{\partial t} = {} & \frac{1}{r}\frac{\partial}{\partial r}\left(K_r r\frac{\partial T}{\partial r}\right) \\ & + \frac{\partial}{\partial z}K_{ax}\frac{\partial T}{\partial z} - v(r)\rho_a\left(c_{p,a}\frac{\partial T}{\partial z}\right) \\ & + \rho_z(1-\varepsilon_b)\frac{\partial}{\partial t}\left(\Delta h_{ads}X\right) - Q_{amb}\end{aligned} \quad (15)$$

Where $c_{p,z}$, $c_{p,ads}$, and $c_{p,a}$ are the specific heat capacity of the zeolite, adsorbed water, and air, respectively; and Q_{amb} is the heat exchange at the reactor wall with the ambient.

In Equation 15, K_r and K_{ax} are the effective direction-dependent radial and axial thermal conductivities of the sorbent bed. Winterberg et al. (2000) describe the radial effective thermal conductivity as a function of radial position r:

$$K_r(r) = \lambda_{bed} + K_{1,h}Pe_\lambda\frac{u_c}{u_0}f(R-r)\lambda_f \quad (16)$$

Here u_0 is the mean axial superficial velocity and u_c is the velocity in the void space, and λ_f is the thermal conductivity of the moist air. In Equation 16, λ_{bed} is packed bed thermal conductivity which is presented in Equation 23. Pe_λ is the molecular Péclet

numbers for heat transfer and can be defined as in Equation 17 (Tsotsas, 2002):

$$Pe_{\lambda} = \frac{u_0 d_s \rho_a c_{p,a}}{\lambda_a} \tag{17}$$

where $c_{p,a}$ is the isobaric specific heat capacity of the gas, and d_s the particle diameter.

In Equation 16, piecewise function $f(R-r)$ can be defined as given in Equation 18:

$$f(R-r) = \begin{cases} \left(\frac{R-r}{k_{2,h} d_s}\right)^2, 0 < R-r \le K_{2,h} d_s \\ 1, K_{2,h} d_s < R-r \le R \end{cases} \tag{18}$$

where R is the bed radius, r is the radial coordinate measured from the centerline. The empirical parameters are defined in Equations 19, 20:

$$K_{1,h} = 0.125 \tag{19}$$

and

$$K_{2,h} = 0.44 + 1\ exp\left(-\frac{Re}{70}\right) \tag{20}$$

With Reynolds number, Re, defined in Equation 21:

$$Re = \frac{\rho_a u_0 d_s}{\mu_a} \tag{21}$$

where, μ_a are the density and dynamic viscosity of the gas phase, evaluated at the local temperature and pressure.

For this annular geometry, the radial effective thermal conductivity can be expressed as given in Equation 22:

$$K_r(r) = \lambda_{bed} + K_{1,h} Pe_{\lambda} \frac{u_c}{u_0} f(R-r) \lambda_a \tag{22}$$

The effective thermal conductivity of the stagnant packed bed, λ_{bed}, is primarily governed by the thermal conductivities of the solid particles λ_s, the fluid λ_a, and the bed porosity ε. For small particle diameters and moderate temperatures $T <$ 300 °C, radiative heat transfer can be neglected (Adler, 2000; Seidel, 1965). In this regime, Zehner and Schlünder (1970) proposed the following correlation for the effective thermal conductivity of a non-flowing packed bed, which accounts for parallel conduction paths through the solid and fluid phases. The Zehner–Schlünder and Zehner–Bauer–Schlünder correlations have been widely validated against experimental data for packed beds of mono-sized spherical particles over broad ranges of porosity and solid–fluid conductivity ratios and are therefore commonly used as a reference model for stagnant-bed thermal conductivity (Qian et al., 2018; Hahne et al., 1991).

$$\lambda_{bed} = \lambda_f \left(1 - \sqrt{1-\varepsilon} + \sqrt{1-\varepsilon} k_c\right) \tag{23}$$

Where ε is the bed porosity, λ_a is the thermal conductivities of the fluid, and k_c is the dimensionless conduction factor in the Zehner–Schlünder correlation for a stagnant packed bed (Zehner and Schlünder, 1970) as defined in Equation 24.

$$k_c = \frac{2}{N}\left(\frac{B}{N^2} k_s - \frac{1}{k_s} \ln\left(\frac{k_s}{B}\right) - \frac{B+1}{2} + \frac{B-1}{N}\right) \tag{24}$$

With k_s defined in Equation 25:

$$k_s = \frac{\lambda_z}{\lambda_a} \tag{25}$$

and N defined in Equation 26.

$$N = 1 - \frac{B}{k_s} \tag{26}$$

Here λ_z is the thermal conductivity of the solid phase. For spherical particles, the deformation parameter B is given in Equation 27.

$$B = 1,25\left(\frac{1-\varepsilon}{\varepsilon}\right)^{10/9} \tag{27}$$

Axial heat transport, K_{ax}, in the sorbent bed is enhanced by thermal dispersion. According to (Tsotsas, 2002), the effective axial thermal conductivity is modeled as a stagnant packed-bed contribution plus a Péclet-based dispersive term, as given in Equation 28:

$$K_{ax} = \lambda_{bed} + \frac{Pe_{\lambda}}{2} \lambda_a \tag{28}$$

4 Numerical methods

The numerical simulations were carried out using COMSOL Multiphysics 6.3, a finite element method (FEM)-based computational fluid dynamics (CFD) platform, to solve the coupled heat and mass transfer equations. User-defined functions were implemented to incorporate reaction kinetics and thermophysical property correlations. Each domain was finely meshed to ensure high spatial resolution and numerical accuracy. In particular, the domains containing the sorbent, where adsorption and desorption processes take place, were meshed with smaller elements, as illustrated in Figure 3a, to accurately capture the steep gradients in temperature and concentration associated with the reactions and coupled heat and mass transfer phenomena. The grid-independence study was conducted on the case with mass flow rate of 80 kg/h and P_w of 25 mbar to confirm that the obtained solutions are independent of the grid resolution. Four different meshes with 30,731, 65,608, 100,547 and 145,020 triangular elements were tested, and the resulting sorbent water loadings were compared. The maximum relative deviation between the meshes with 100,547 and 145,020 elements did not exceed 0.02%. The grid-independence verification is shown in Figure 3b. Consequently, the grid with 100,547 elements was selected for all subsequent simulations as a good compromise between accuracy and computational cost.

A second-order quadratic scheme was employed for the discretization of all governing equations. Although the global time step was limited to a maximum of 1 s, the solver automatically reduced the initial time step significantly to facilitate stable convergence at the beginning of the simulation.

4.1 Definition of the boundary conditions and assumptions

The model represents the zeolite reactor bed along with its surrounding walls, including the metallic structure and insulation.

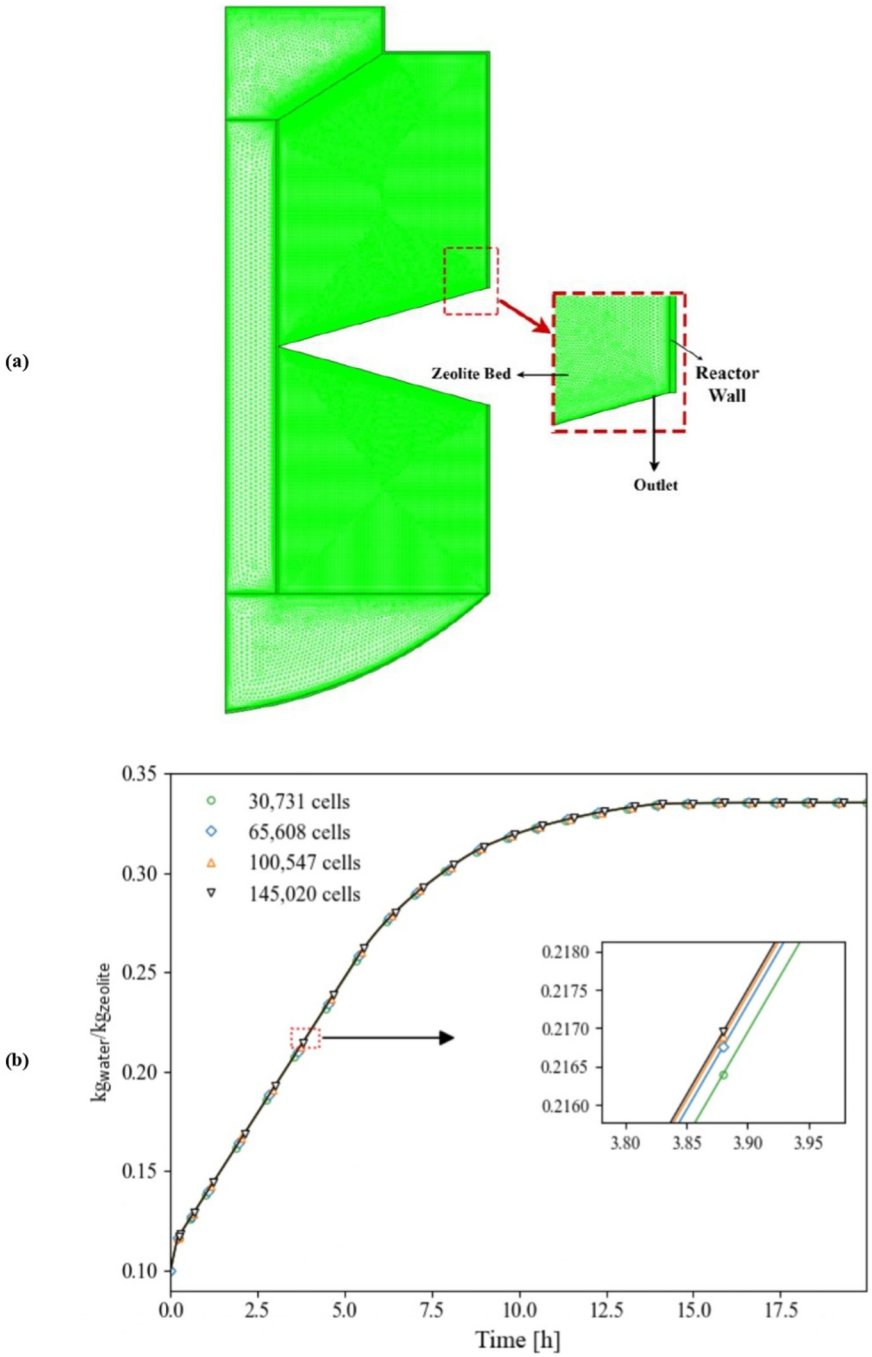

FIGURE 3
The quality of computational meshes: **(a)** computational mesh; **(b)** grid-independence results for different mesh sizes.

The reactor contains solid sorbent and moist air. The solid phase comprises the sorbent material (denoted by subscript z) and the adsorbed water, while the fluid phase consists of a mixture of dry air (subscript a) and water vapor (subscript w). Therefore, two phases—solid and gas—are taken into account within the reactor.

The following key assumptions are considered for the numerical simulations.

- The packed bed of sorbent particles was modeled as a homogeneous porous medium with effective material properties, neglecting microscale pellet structures.
- The model assumes thermal equilibrium between the solid matrix and the gas phase, enabling the use of a single energy equation.
- To account for local density variations, humid air was modeled as a weakly compressible flow.

- Radiative heat transfer within the reactor domain or to the surroundings was assumed to be negligible.
- As the fluid's absolute pressure remains below 0.1 MPa, both components of the moist air—water vapor and dry air—are treated as ideal gases.
- The particles are assumed to have uniform size, shape, and porosity.
- All material properties are temperature dependent.

The boundary conditions applied in the model are defined as follows:

- The inlet flow enters at a constant temperature, which is assumed to be equal to the ambient environmental temperature.
- The moisture content of the incoming air is fixed and determined based on the specified relative humidity or the corresponding partial pressure of water vapor. The inlet relative humidity was converted to a water-vapor mass fraction at the given inlet temperature, and this mass fraction was imposed as the species boundary condition at the gas inlet.
- At the outlet, zero-gradient boundary conditions are imposed for water vapor loading, $\frac{\partial w}{\partial r} = 0, \frac{\partial w}{\partial z} = 0$.
- The temperature gradient is zero at the outlet ($\frac{\partial T}{\partial r} = 0, \frac{\partial T}{\partial z} = 0$).
- Heat loss to the environment is considered using the expression given in Equation 29:

$$Q_{amb} = U(T_{amb} - T) \tag{29}$$

Where U is the overall heat transfer coefficient, and can be calculated based on Equation 30:

$$U = \frac{1}{R_{tot} A_{ht}} \tag{30}$$

Where A_{ht} is the heat transfer area, and R_{tot} is the overall thermal resistance, which consists of four components: Convective resistance between the air inside the reactor and the reactor wall, conductive resistance of the reactor wall, conductive resistance of the insulation layer, and convective resistance between the insulation surface and the surrounding environment. The sum of these resistances can be expressed as (Gao et al., 2023):

$$R_{tot} = \frac{1}{2h_m \pi R_1} + \frac{1}{2\pi k_{ss}} ln\left(\frac{R_2}{R_1}\right) + \frac{1}{2\pi k_{ins}} ln\left(\frac{R_3}{R_2}\right) + \frac{1}{2h_{amb} \pi R_3} \tag{31}$$

Where h_m, h_{amb} are the convective heat transfer coefficients at the reactor's inner metal wall and at the outer insulation surface, respectively. R_1, R_2, and R_3 represent the inner radius of the reactor, the outer radius of the reactor wall, and the outer radius including insulation, respectively.

K_{ss} and K_{ins} in Equation 31 are the thermal conductivities of the metal wall and the insulation.

The main operating parameters and initial conditions used in the numerical simulations are listed in Table 3. The corresponding flow, species-transport, and heat-transfer boundary conditions applied in the CFD model are summarized in Table 4.

TABLE 3 Assigned values for the initial and boundary conditions.

Parameter	Value	Unit	Description
MFR	50–120	$\frac{kg}{h}$	Mass flow rate of air
P_w	5–25	mbar	Partial pressure of water vapor
T_{amb}	30	°C	Ambient temperature
T_{in}	20–50	°C	Temperature of inlet air
$X_{init,\ Ads}$	0.1	$\frac{kg_{water}}{kg_{zeolite}}$	Initial loading

4.1.1 Model limitations

The present model involves simplifying assumptions that impose limitations but can be considered acceptable for the operating conditions studied. This section discusses the limitations of the current model. First, a local thermal equilibrium (LTE) formulation with a single energy equation while using direction-dependent effective thermal conductivities in the radial and axial directions, based on Winterberg et al. (2000) and Zehner–Schlünder-type correlations (Zehner and Schlünder, 1970). The bed is modelled as a homogeneous porous medium with a single representative particle size. Local packing inhomogeneities and porosity variations are not resolved explicitly. Radiative heat transfer is neglected because particle diameters are small and temperatures remain below about 300 °C (Adler, 2000; Seidel, 1965; Zehner and Schlünder, 1970), for which conduction and dispersion clearly dominate the overall heat transport in the bed. In the gas phase, water vapor is treated as an ideal gas. This is consistent with standard psychrometric practice, where moist air is modelled as a mixture of ideal gases (dry air and water vapor) at near-atmospheric pressures. At the operating conditions of the present sorption storage system (bed temperatures of around 100 °C and total pressure close to 1 bar), water vapor is far from the critical region and its non-ideality is small: virial-equation data show that the compressibility factor Z deviates from unity by only a few percent in this range, so that the ideal-gas equation provides an adequate representation of the vapor phase (Cengel and Boles, 2002; Tenny and Cooper, 2017).

4.2 Validation

To validate the accuracy of the developed numerical simulation, its results were compared against experimental data from Mette et al. (2014a) Figure 4a. In this setup, a stainless-steel fixed-bed reactor, wall thickness 3 mm, inner diameter 50 mm, and height 127 mm, serves as the experimental unit. It is filled with binder-free zeolite 13X and wrapped with 80 mm of mineral wool for thermal insulation. In the experimental procedure, compressed air is first passed through an oil separator and drying unit. A controlled mass flow rate of 1 kg/h, with a measurement accuracy of ±1.4%, is set using a mass flow controller. The airflow is then split, with one part routed through a humidifier while the other bypasses it. By adjusting the bypass using a control valve, the desired humidity level is achieved. The humidified air is subsequently heated to the target inlet temperature before entering the reactor, where the

TABLE 4 Summary of flow, species, and heat-transfer boundary conditions used in the CFD model.

Region	Type	Description
(a) Flow boundary conditions		
Inlet face	Inlet boundary	Mass flow rate
Outlet face	Outlet boundary	Pressure outlet
Walls	Default wall	No-slip, impermeable walls
(b) Species boundary conditions		
Inlet	Inflow	Water vapor content derived from partial pressure ($P_w = 5 - 25\,mbar$); implemented as water mass fraction
Outlet	Outflow	
Sorbent bed	Reaction source	$(1-\varepsilon_b)\frac{\rho_z}{\rho_a}\frac{\partial X}{\partial t}$
Walls	No-flux	Impermeable to species
(c) Heat-transfer boundary conditions		
Inlet	Inflow, T_{in}	Gas inlet temperature ($T_{in} = 20 - 50\,°C$)
Outlet	Outflow	
Sorbent bed	Heat source	$\rho_z(1-\varepsilon_b)\frac{\partial}{\partial t}(\Delta h_{ads} X)$
Outer wall/insulation	Convective heat flux	Natural convection to ambient

adsorption process occurs. As adsorption proceeds, the released heat raises the temperature of the air, resulting in a higher outlet temperature. Dew point measurements at both the inlet and outlet were used to determine the air humidity, while thermocouples installed at various vertical positions within the reactor recorded the temperature profile.

To validate the numerical model, its predictions were compared with data from the reference experiments. The comparison covered two main quantities: (i) the outlet air temperature for different inlet water-vapor partial pressures and (ii) the transient temperature evolution of the sorbent bed at two axial positions. In addition, key performance indicators were evaluated, namely the maximum temperature lift $\Delta T_{\max}$, the change in water loading, the volumetric energy density q_{vol}, and the mean adsorption enthalpy $\Delta h_{\mathrm{ads,m}}$. The agreement between experiments and simulations was quantified using the mean absolute error (*MAE*) and the mean absolute percentage error (*MAPE*), as defined in Equations 32, 33.

$$MAE = \frac{1}{N}\sum_{i=1}^{N}\left|T_{\mathrm{sim},i} - T_{\mathrm{exp},i}\right| \tag{32}$$

$$MAPE = \frac{100}{N}\sum_{i=1}^{N}\left|\frac{T_{\mathrm{sim},i} - T_{\mathrm{exp},i}}{T_{\mathrm{exp},i}}\right| \tag{33}$$

The first quantity analysed was the outlet air temperature. The comparison was carried out at sensor $T_{\mathrm{R,1-4}}$, which is located in the centre of the packed bed ($r = 0$) at an axial position $z = 0.125$ above the sieve at the bottom of the bed (Mette, 2014b). The time evolution of the experimental and simulated temperature at this sensor for inlet water-vapor partial pressures of 5, 15 and 25 mbar is shown in Figure 4a. At this location, the experimental and simulated outlet temperatures are denoted by $T_{\mathrm{exp},i}$ and $T_{\mathrm{sim},i}$ at the i-th measurement time, respectively, and N is the total number of data points. For the higher pressures $P_w = 15$ and $P_w = 30$ mbar, the outlet sensor $T_{R,1-4}$ shows *MAE* of about 2.4 °C and 6.8 °C, and *MAPE* of about 4.8% and 10.1%, respectively.

The transient model was validated also against measured bed temperatures at two thermocouples located on the bed centreline ($r = 0$) at axial positions $z = 0.055$ m (point P1) and $z = 0.095$ m (point P2). For point P1 ($r = 0, z = 0.055m$), the comparison of simulation results with experimental data yields an *MAE* of 2.42 °C and an *MAPE* of 4.88%. For point P2 ($r = 0, z = 0.095m$), the *MAE* is 1.740 °C and *MAPE* is 3.96%. The time evolution of experimental and simulated temperatures in these two points is illustrated in Figure 4b.

Moreover, four main quantities measured in the experiments: the maximum temperature lift ΔT_{max}, the change in sorbent loading Δ_X, which represents the water uptake rate, the volumetric energy density q_{vol}, and the mean adsorption enthalpy $\Delta h_{ads,m}$, representing the adsorption kinetics. The simulated $\Delta T_{\max}$ is 36.14 °C, while the experiment gives 38.3 °C, which represents a deviation of about 2.2 °C (≈5.6%). The measured loading change is 0.247 $kg_{water}/kg_{zeolite}$ and the simulation predicts 0.244 *kg/kg*, which is about 1.2% lower. The volumetric energy density is 159.3 kWh/m^3 in the experiment and 154.2 kWh/m^3 in the simulation (difference ≈3.2%), and the mean adsorption enthalpy is 3,210 *kJ/kg* in the experiment compared to 3,134.66 *kJ/kg* in the simulation (difference ≈2.3%). The good agreement between simulated and measured values for both local state variables and performance metrics confirms that the model reliably represents the coupled heat and mass transfer and the reaction kinetics in the reactor.

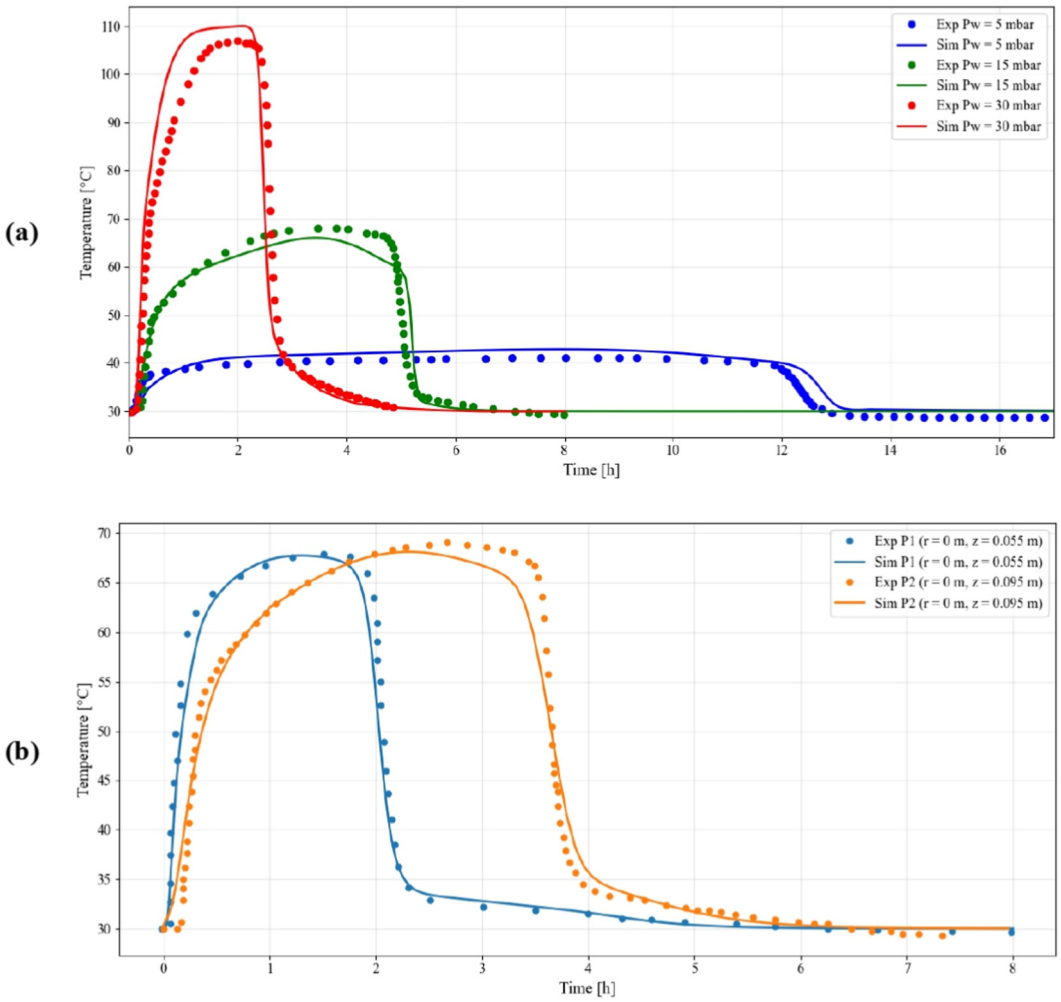

FIGURE 4
Validation of the developed simulation at T_{ads} = 30 °C **(a)** under different partial pressures **(b)** by comparing temperatures at two locations in the packed bed.

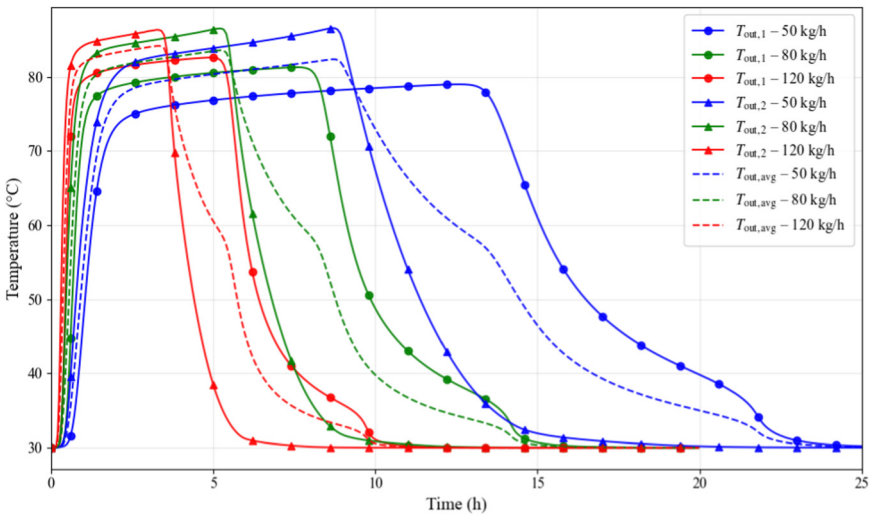

FIGURE 5
Outlet temperatures ($T_{out,1}$; $T_{out,2}$, and $T_{out,avg}$) vs. time for different air mass flow rates (inlet temperature = 30 °C, water partial pressure = 25 mbar).

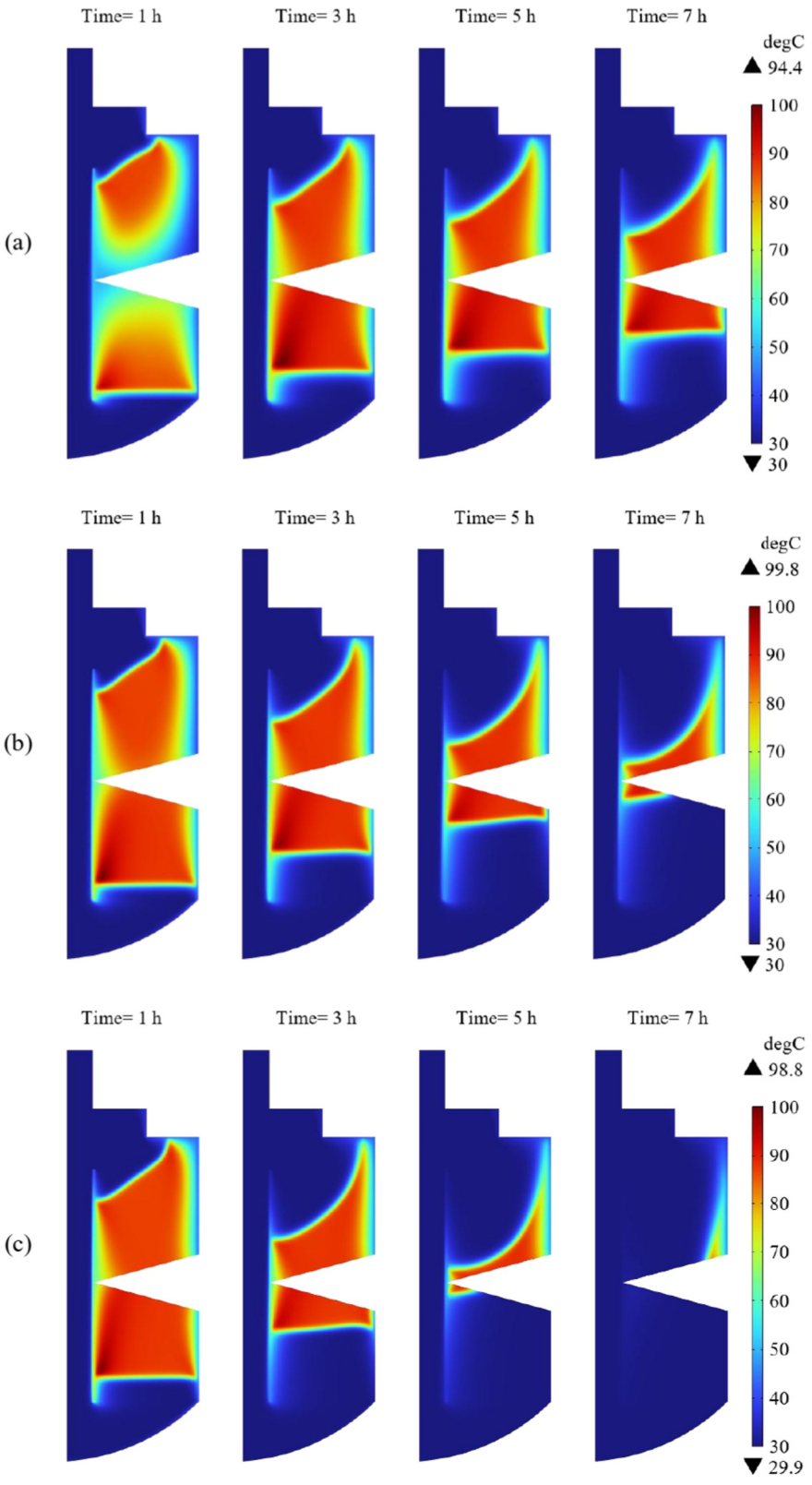

FIGURE 6
Influence of mass flow rate on zeolite bed temperature evolution: **(a)** 50 kg/h, **(b)** 80 kg/h, **(c)** 120 kg/h.

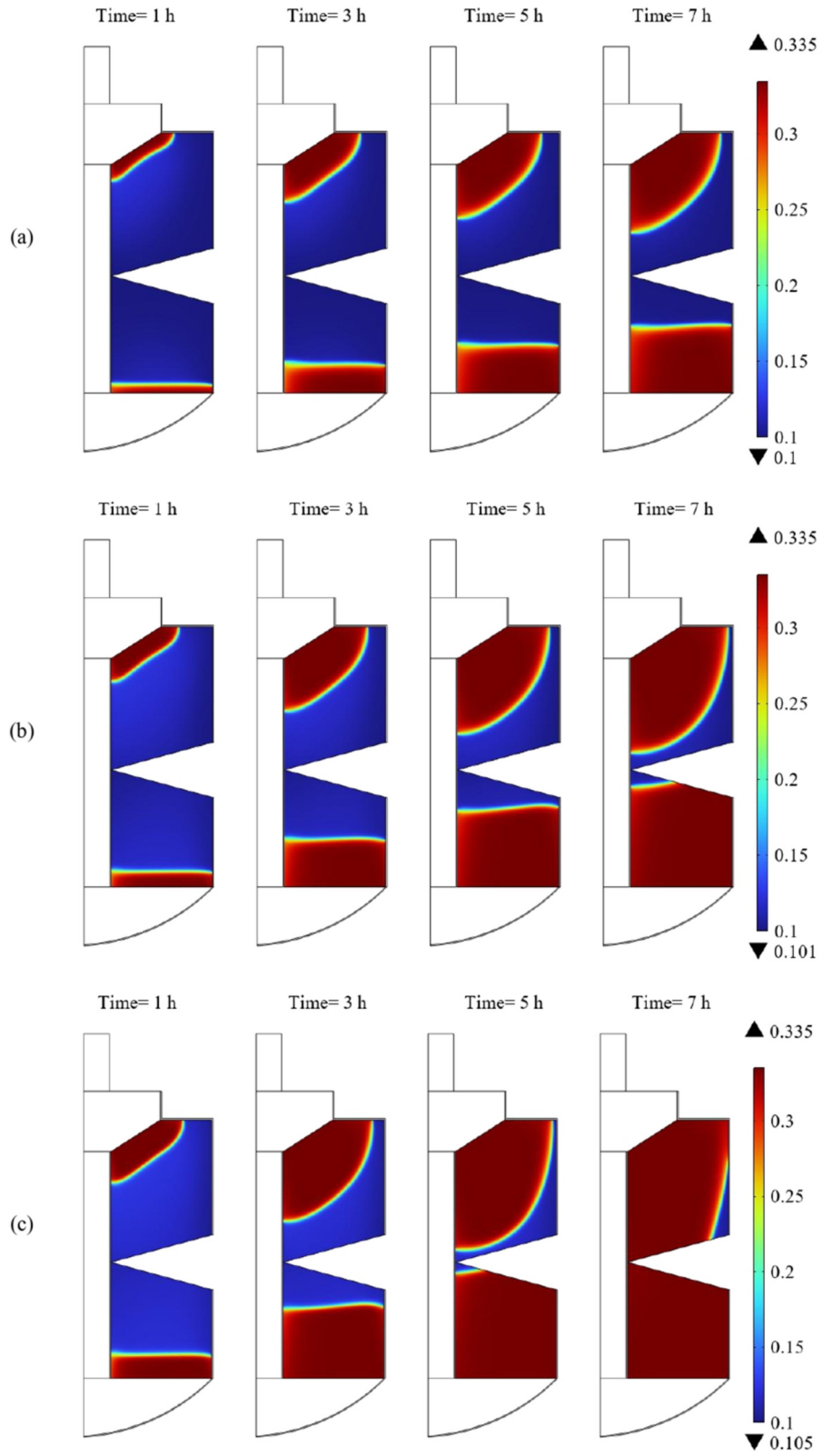

FIGURE 7
Influence of mass flow rate on zeolite water uptake: **(a)** 50 kg/h, **(b)** 80 kg/h, **(c)** 120 kg/h.

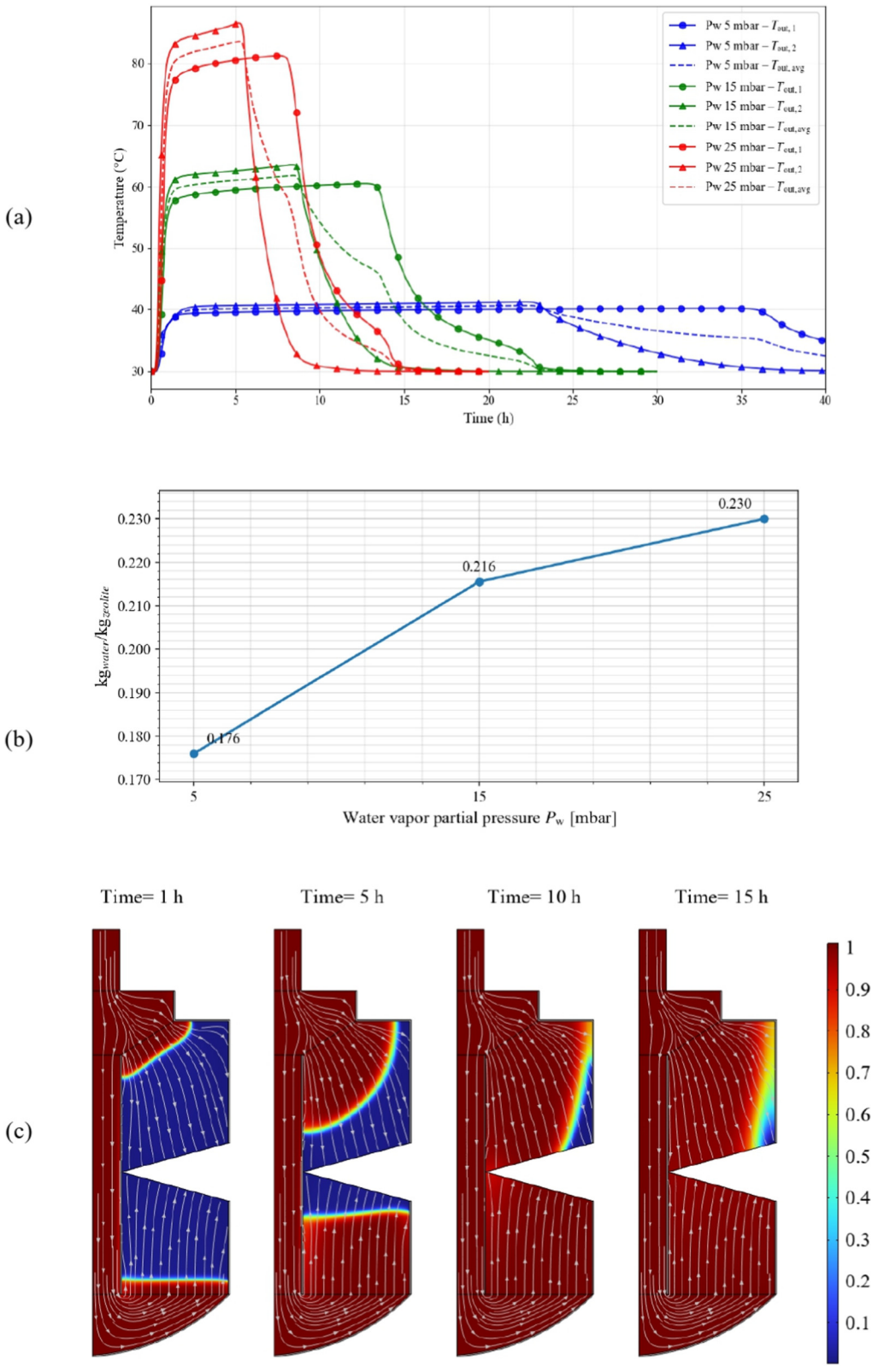

FIGURE 8
The influence of the partial pressure of water in the inlet air flow **(a)** on the output temperature **(b)** on the water uptake of the bed under different pressures of 5 mbar, 15 mbar, and 25 mbar **(c)** Sorption-Wave Propagation: C_{H2O} and Total Molar-Flux Streamlines (Mass flow rate of 80 kg/h and Pw = 25 mbar).

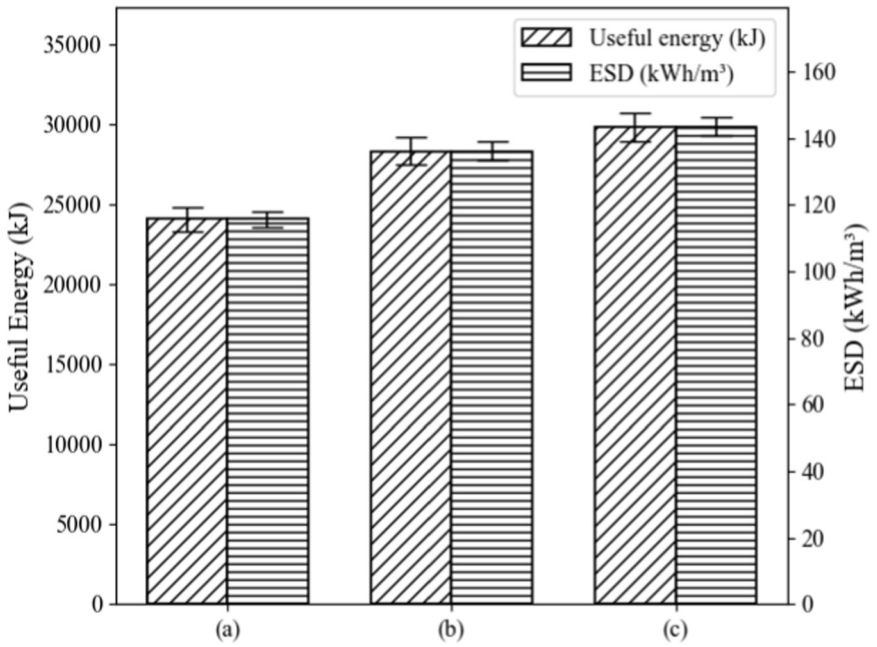

FIGURE 9
Comparison of useful energy and energy storage density for partial pressure of (a) 5 mbar, (b) 15 mbar, (c) 25 mbar.

It should be mentioned that the segmented modular reactor analyzed in this work has not yet been validated experimentally. The model is calibrated and validated against the fixed-bed reactor experiments of Mette et al. (2014a) with the same material and similar operating conditions, which supports the underlying descriptions of sorption equilibrium, kinetics and heat–mass transfer. However, the performance indicators reported for the segmented reactor are based solely on numerical predictions.

5 Performance evaluation

To assess the performance of the reactor several metrics are defined: amount of useful stored thermal energy extracted from the reactor, outlet temperature, and energy density. The performance of the energy storage system is assessed during the adsorption process, using 30 °C as the reference temperature. During the process, water vapor is absorbed by zeolite, releasing both bonding and condensation enthalpy. Part of this released heat is transferred to the air flow, while the rest is lost to the environment through the reactor walls. Additionally, a portion of the energy is used as sensible heat to raise the bed temperature during the process. The overall energy balance during adsorption is given in Equation 34.

$$\int_0^t \dot{m} c_{p,a}\left(T_{Ads,out} - T_{Ads,in}\right) + Q_{los,Ads} + \sum m_s c_{p,z}\left(T_{Ads} - T_0\right) = Q_{z,Ads} \tag{34}$$

In the above equation, t is the total duration of the adsorption phase, $\dot{m}$ is the mass flow rate of air, and $c_{p,a}$ and $c_{p,z}$ are the specific heat capacities of the air and the zeolite, respectively. $T_{Ads,in}$ and $T_{Ads,out}$ are the inlet and outlet temperatures of air during the adsorption process. $Q_{los,Ads}$ represents the heat losses during the process, and $Q_{z,Ads}$ is the heat released by adsorption.

The energy storage density (ESD) of the system, expressed in kWh/m^3, is defined as the ratio of the recovered usable heat to the volume of the zeolite used, as given in Equation 35.

$$ESD = \frac{\int_0^t \dot{m} C_{p,a}\left(T_{Ads,out} - T_{Ads,in}\right) dt}{Volume\,of\,zeolite} \tag{35}$$

6 Results and discussion

This section presents the performance of the designed reactor based on numerical investigations. The key parameters influencing the processes are air flow rate, inlet temperature, and relative humidity. The simulation results are discussed in terms of water uptake, water concentration and temperature variations, useful energy, energy density, and pressure drop. Except in Section 6.3, where the influence of the initial bed temperature and inlet air temperature is investigated, an initial uniform bed temperature of 30 °C and an initial water loading of 0.1 $kg_{water}/kg_{zeolite}$ are assumed at the beginning of the discharge process. First, the performance of the initial design was evaluated under varied boundary conditions; based on these findings, the design was subsequently improved.

6.1 The influence of the mass flow rate of the air

The outlet behavior is strongly controlled by the air mass flow rate. Humid air at 30 °C and 60% relative humidity (P_w = 25 mbar) is supplied to the bed with mass flow rates of 50, 80, and 120 kg/h. Figure 5 shows the influence of the air mass flow rate on the

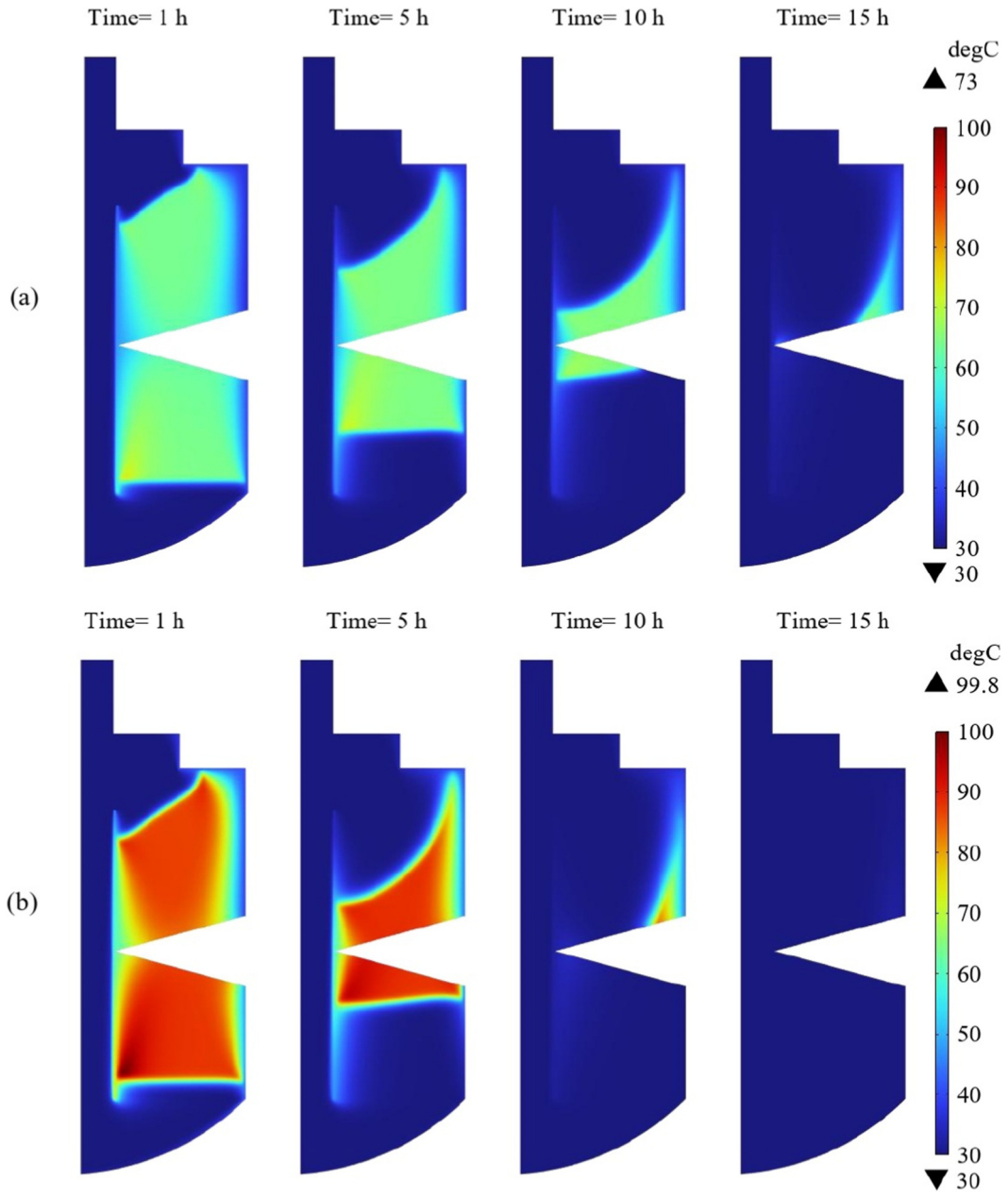

FIGURE 10
The variation of temperature inside the reactor with changing vapor partial pressure **(a)** 15 mbar and **(b)** 25 mbar.

discharge temperature of the module. Outlet 1 denotes the outlet of the upper segment and Outlet 2 the outlet of the lower segment. The "average outlet temperature" is defined as the mean of both outlet temperatures. The locations of Outlet one and Outlet 2 are indicated in Figure 2.

At the lowest flow rate (50 kg/h), both Outlet one and Outlet 2 maintain a peak outlet temperature for a long time, followed by a slow decline over the discharge period. The low flow rate gives the air a long residence time in bed, so the adsorption front moves slowly through the sorbent. As a result, the discharge is long, and the average outlet temperature remains relatively high and stable.

At 80 kg/h, the stronger convective heat removal causes a faster decrease in $T_{out,1}$ and $T_{out,2}$. The outlet temperature peaks (approximately 85 °C at Outlet 1 and 80 °C at Outlet 2) are reached earlier than at 50 kg/h, but the period during which the outlet temperature remains in a useful range is clearly shorter. At the highest tested flow rate (120 kg/h), maximum outlet temperatures of about 85 °C at Outlet 1 and 82 °C at Outlet 2 are reached quickly, but both $T_{out,1}$ and $T_{out,2}$ then decrease rapidly, and the useful temperature range drops significantly within the first few hours. This steep temperature drop is a direct consequence of strong convective cooling and rapid depletion of the stored thermal energy.

As shown in Figure 5, the effect of the mass flow rate is more pronounced at Outlet 1 (upper outlet). At Outlet 2 (lower segment), almost the same peak outlet temperature is obtained for all flow rates, which is consistent with the more uniform flow distribution

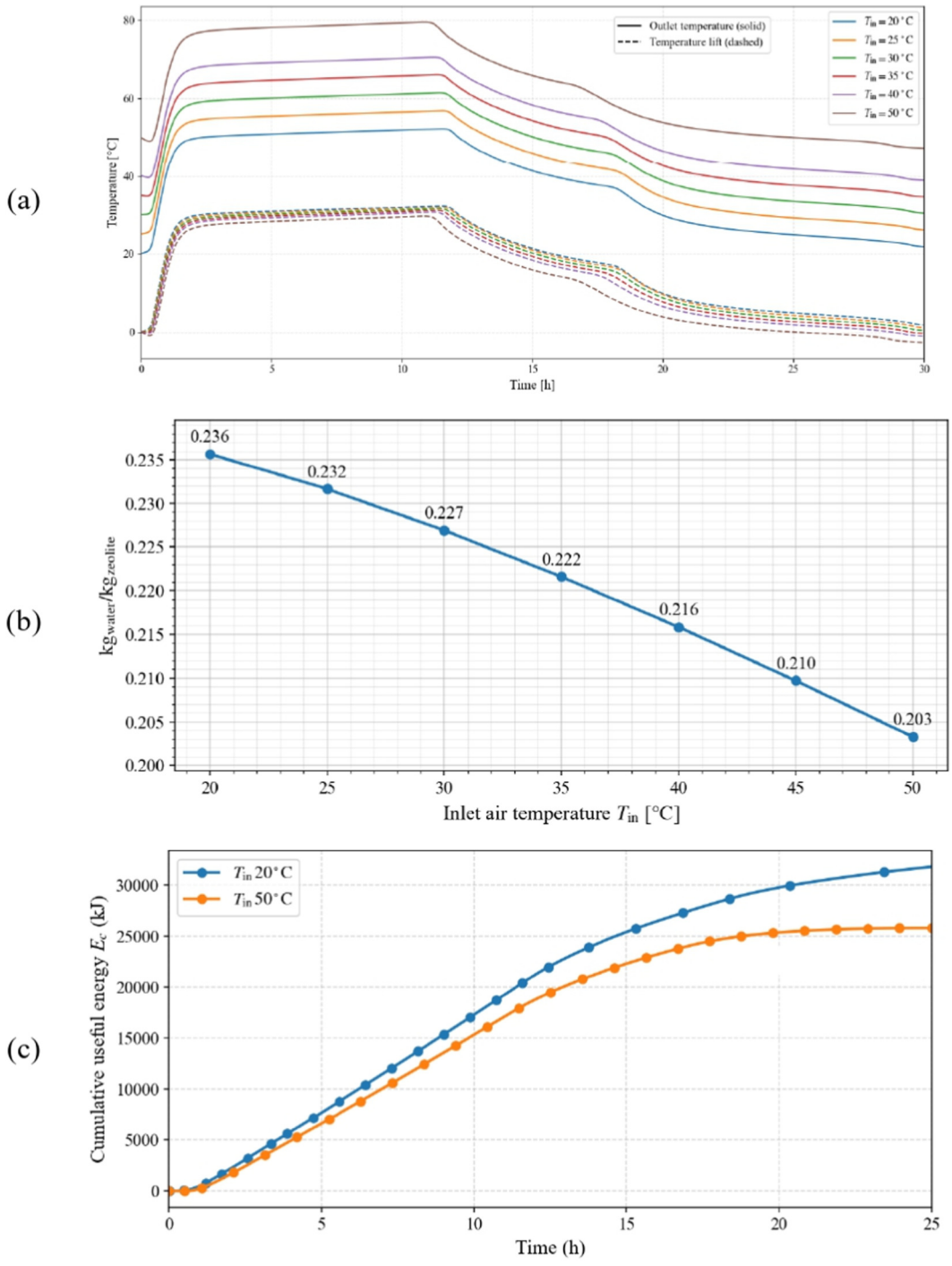

FIGURE 11
(a) Effect of inlet air temperature on outlet air temperature and temperature lift. **(b)** Water uptake of the bed under different inlet temperatures. **(c)** Cumulative thermal energy released during adsorption for different inlet air temperatures.

in this region; only the discharge duration varies, as expected for different mass flow rates. In the upper section, however, increasing the mass flow rate directly affects the maximum outlet temperature because the gas follows a direct inlet–outlet path. As the flow rate increases, the residence time of the air in the upper bed decreases, reducing the contact with the zeolite and thereby lowering the maximum outlet temperature in this region.

The hydraulic penalty also increases with flow rate: the static pressure drop rises from 71 Pa at 50 kg/h to 123 Pa at 80 kg/h and about 203 Pa at 120 kg/h. These results highlight a clear trade-off between long, stable heat delivery with low pressure drop (low flow) and high power output with higher fan energy demand (high flow). For system control, two key targets are the outlet temperature level and the discharge time (duration above a required temperature).

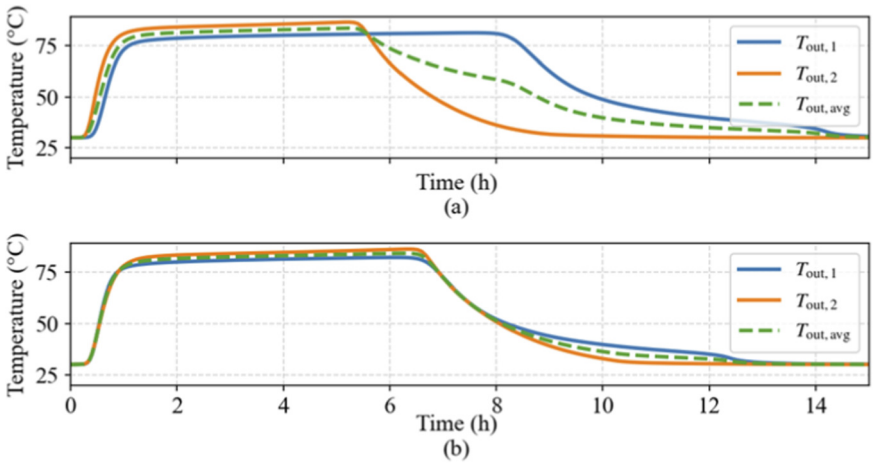

FIGURE 12
Temperature fields over discharge [**(a)** before improvement, **(b)** after].

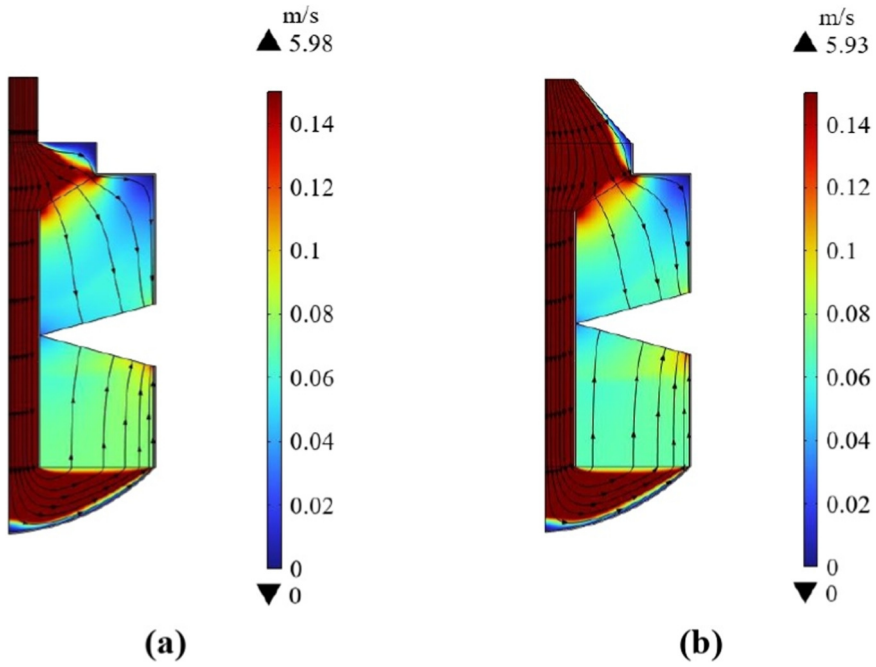

FIGURE 13
Velocity distributions inside the bed: **(a)** first design, **(b)** improved design.

The results show that both quantities, together with the delivered power, can be adjusted simply by changing the air mass flow rate, making the flow rate an effective control variable for operating the storage module.

The influence of the mass flow rate on the temperature profile inside the reactor is presented in Figure 6. At 50 kg/h, the longer residence time allows the adsorption front to penetrate deeper into the bed, resulting in more uniform heating and better overall utilization of the storage material. With increasing flow rate, the discharging process becomes shorter, and the temperature peaks occur earlier, but the high-temperature period is reduced.

Based on the thermal analysis of the discharging process for the three mass flow rates, the useful thermal energy transferred to the air, changes only slightly: 8.28 kWh at 50 kg/h, 8.24 kWh at 80 kg/h, and 8.12 kWh at 120 kg/h. At 50 kg/h the losses are about 0.67 kWh, which is relatively high due to the long discharge time. At 80 kg/h the losses decrease to 0.45 kWh, and at 120 kg/h they fall further to 0.32 kWh. The increase in heat losses at lower flow rate is therefore linked to the longer discharging period, which provides more time for heat to be lost to the surroundings. In real applications, these losses can be higher, depending on the ambient temperature and the discharge duration.

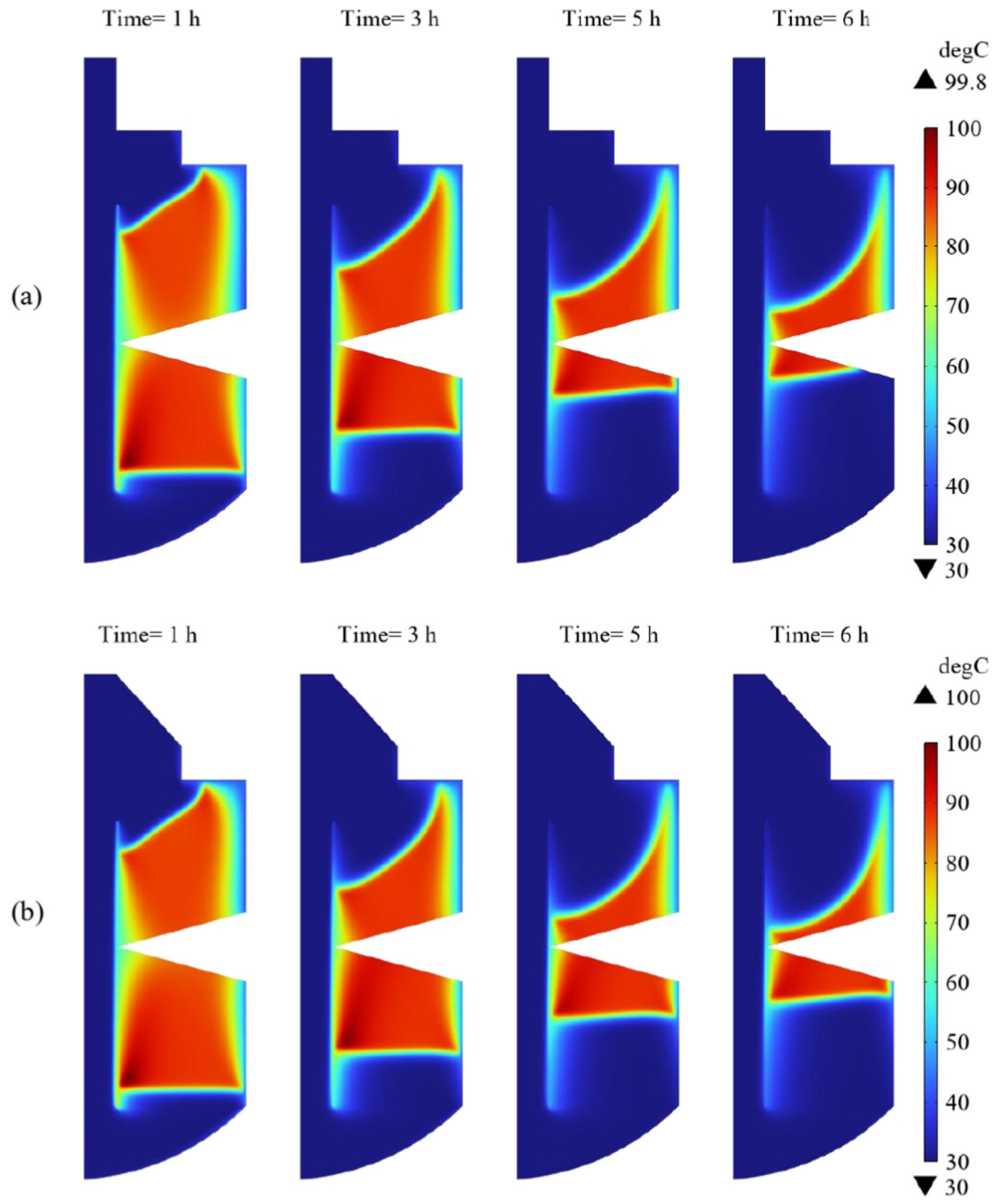

FIGURE 14
Variation of outlet temperature histories $T_{out,1}$, $T_{out,2}$, $T_{out,avg}$: **(a)** first design, **(b)** improved design.

For a zeolite bed volume of 57.5 L, the energy storage densities (ESD) are 144 kWh/m^3, 143.3 kWh/m^3, and 141.2 kWh/m^3 for mass flow rates of 50, 80, and 120 kg/h, respectively. This shows that the flow rate has only a minor influence on energy density, but a significant influence on the maximum achievable power and outlet temperature. For the energy calculations, the stopping criterion for the adsorption process was an outlet temperature of 35 °C, corresponding to a temperature lift of 5 K above the inlet air (30 °C). Below this threshold, the driving temperature difference to the surroundings is small, the useful heat output and exergy content are low, and the remaining discharge mainly consists of a long low-power tail. Using 35 °C as a cutoff therefore ensures a consistent comparison of the different operating cases with respect to both energy and discharge time.

The effect of the mass flow rate on the water uptake of zeolite is presented in Figures 7a–c. At higher mass flow rates, the rates of heat and mass transfer increase, which accelerates the adsorption reaction. As a result, water uptake proceeds more rapidly, and a larger portion of the bed becomes saturated in a shorter time. In contrast, at a mass flow rate of 50 kg/h, even after 7 hours, a

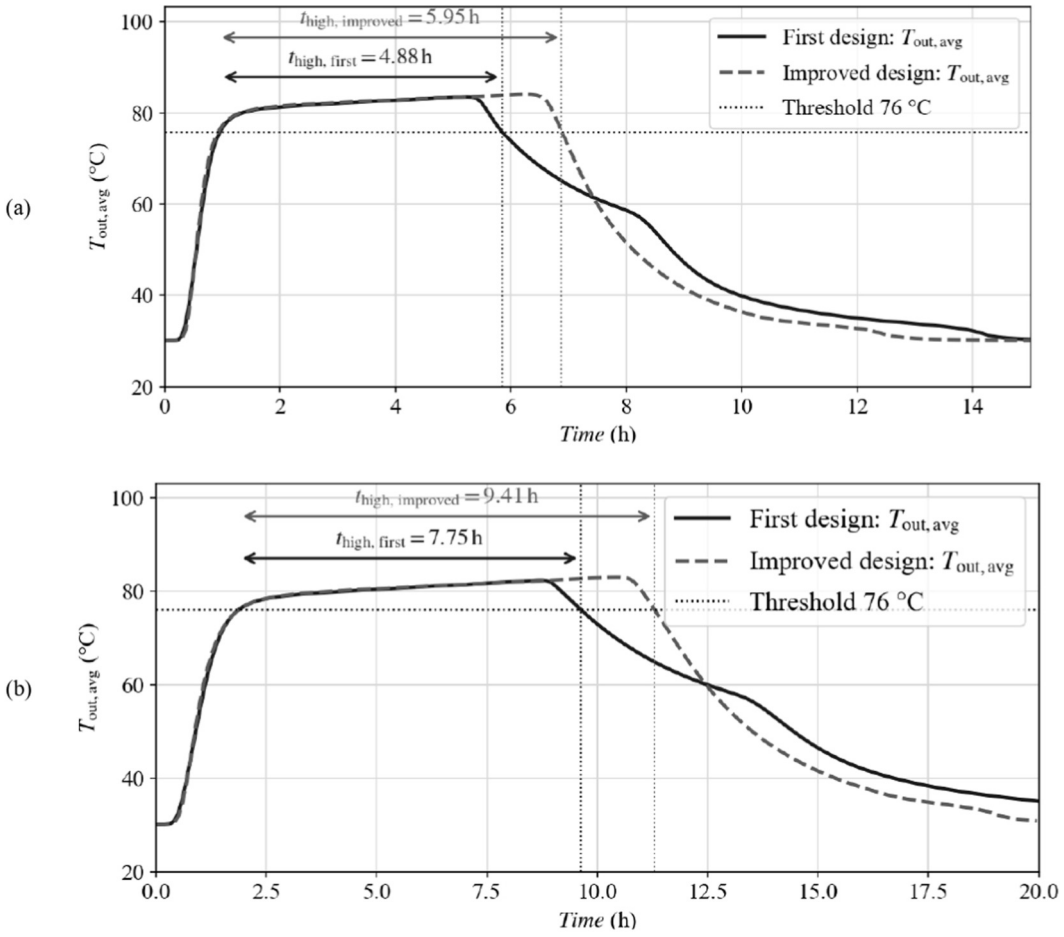

FIGURE 15
Average outlet temperature and duration of maximum temperature for baseline and improved reactors **(a)** 80 kg/h, **(b)** 50 kg/h.

significant part of the bed has not yet fully adsorbed water, and the adsorption front has not completely reached the outlet.

6.2 The influence of the relative humidity of the air on the performance of the reactor

Another important factor influencing the efficiency of the adsorption process, and consequently the attainable outlet temperature, is the partial pressure of water vapor in the humid air entering the reactor. To assess its impact, simulations were performed for three partial pressures: 5, 15, and 25 mbar at the same mass flow rate of 80 kg/h and an inlet temperature of 30 °C.

Figure 8a presents the variation of temperature over one cycle for three operating pressures of 5, 15, and 25 mbar. Higher partial pressure yields a higher peak temperature but a shorter delivery time: at 25 mbar (red) the outlets rise quickly to ~80 °C–85 °C and return to ~30 °C by ~13 h; at 15 mbar (green) they plateau near ~60 °C–63 °C and decay to ambient by ~22–24 h; at 5 mbar (blue) they stabilize around ~40 °C–41 °C and remain elevated for > 30 h before declining.

Figure 8b shows the water uptake amount under different water-vapor partial pressure P_w under otherwise identical conditions. Adsorption was terminated when the outlet gas temperature reached 35 °C; both water uptake and the useful energy were evaluated at this cut-off. The capacity increases monotonically with P_W: at 5 mbar, 0.176 $kg_{water}/kg_{zeolite}$, at 15 mbar, 0.216 $kg_{water}/kg_{zeolite,}$ and at 25 mbar case 0.23 $kg_{water}/kg_{zeolite}$. The cut-off occurred for P_w = 5 mbar after approximately 35 h of adsorption, for P_w = 15 mbar after ≈17 h, and for P_w = 25 mbar after about 12 h. This behavior is consistent with the Dubinin–Astakhov (D–A) isotherm model: increasing water-vapor pressure leads to higher equilibrium loadings and a larger difference between local and equilibrium loading, which increases the mass-transfer driving force in the LDF description, accelerates vapor uptake and produces a stronger temperature rise in the bed, bus also faster discharge.

Figure 8c presents the time evolution of the gas-phase water concentration C_{H2O} (mol/m^3) in the reactor. White streamlines show the total molar flux of water and the transport paths from the vapor channel into the porous beds. A high-concentration boundary layer forms at the channel–bed interface and advances into the beds as a curved sorption wave; the upper bed is reached earlier, while the lower bed lags; however, the process in the lower bed finishes earlier. The peak gas-phase concentration approaches ≈0.60 mol/m^3; locally, where the zeolite becomes saturated, the gas concentration tends to this value. The same qualitative behavior is

observed at other partial pressure rates, but with different rates of progress in time.

The partial pressure of water vapor governs the adsorption driving force and thus directly affects the adsorption dynamics and overall thermal performance of the storage system. A higher partial vapor pressure increases the concentration gradient between the humid air and the sorbent material, enhancing the water vapor uptake rate during the discharge phase. This accelerates and intensifies the adsorption reaction, resulting in higher heat release and improved useful thermal output. The results of energy analysis are presented in Figure 9. Raising the inlet vapor pressure from 5 mbar to 15 mbar and to 25 mbar increased the energy density from 115.6 kWh/m^3 to 136.04 kWh/m^3 and 143.3 kWh/m^3, respectively.

The simulation results also show how the inlet water-vapor partial pressure affects the temperature field in the sorption bed. At the lower vapor partial pressure of 15 mbar (Figure 10a), the reduced driving force for mass transfer at low P_w limits the peak bed temperature to around 60 °C, which in turn results in a lower outlet peak temperature, as seen in Figure 8a. In contrast, at P_w = 25 mbar, the sorption proceeds more intensively, releasing more heat in a shorter time and leading to higher bed temperatures and faster front propagation. However, as illustrated in Figure 10b, the bed is then discharged more quickly, in agreement with the more rapid decrease in outlet temperature observed in Figure 8a.

In summary, According to the Dubinin–Astakhov model, increasing p_w from 15 to 25 mbar reduces the adsorption potential A and thereby increases the equilibrium uptake W^*, which explains the higher water loading and bed temperatures observed at 25 mbar compared to 15 mbar.

6.3 The influence of adsorption temperature

The impact of the inlet temperature of the humid air and the initial bed temperature on the discharging process is investigated in this section. In all cases, humid air with a water vapor partial pressure of 15 mbar and a mass flow rate of 60 kg/h is supplied to the reactor with initial water loading of 0.08 $kg_{water}/kg_{zeolite}$, while the inlet air temperature and initial bed temperature are varied between 20 °C and 50 °C. For this fixed vapor partial pressure, the corresponding relative humidity decreases from about 64% at 20 °C to about 12% at 50 °C (at atmospheric pressure).

Figure 11a presents the effect of the inlet temperature of the incoming airflow on the outlet temperatures and temperature lift. When the inlet temperature is lower, the maximum achievable bed temperature during adsorption is also lower; however, the temperature lift is observed to be slightly higher. According to the Dubinin–Astakhov (DA) equation, a decrease in adsorption temperature increases the equilibrium uptake of water vapor by zeolite, leading to higher temperature lift. This is reflected in the simulated water uptakes of 0.236 $kg_{water}/kg_{zeolite}$ for 20 °C, compared to 0.2 for 50 °C, as can be seen in Figure 11b. The higher uptake at lower temperature enables a larger quantity of water to be adsorbed, thereby releasing a greater amount of sorption heat over the course of the discharging phase. Although the outlet temperatures are lower than in the high-temperature inlet cases, the total sorption released energy is greater due to the higher mass of water adsorbed. Conversely, for higher inlet temperatures, the bed reaches higher peak temperatures early in the adsorption phase. However, the elevated temperature reduces the adsorption potential of zeolite, limiting total water uptake and, consequently, cumulative heat release, despite the higher short-term outlet temperature. It should be noted that the inlet air temperature can be adjusted according to the desired outlet temperature.

Figure 11c shows the cumulative thermal energy released during the adsorption (discharging) phase for inlet air temperatures of 20 °C and 50 °C, with a vapor partial pressure of 15 mbar and a mass flow rate of 60 kg/h. The results indicate that lower inlet air temperatures lead to higher total recovered energy, consistent with the higher adsorption capacity of zeolite at reduced temperatures. The case with T_i = 20 °C delivers the largest cumulative energy output, confirming that reduced adsorption temperature enhances water uptake and total thermal energy release.

6.4 Improving performance through design improvement

Simulation results for the initial configuration show that the two packed-bed segments do not behave in the same way. The upper and lower sections reach their peak temperature and maximum adsorption at different times and cool down over different intervals. Consequently, one segment completes the discharge earlier, so both outlets do not provide useful heat over the same period. In addition, a noticeable temperature difference arises between the two outlet streams, which lowers the average outlet temperature and causes an early drop at the primary outlet. Together, these effects reduce the effective utilisation of the storage material and degrade overall system performance. This behaviour motivated a redesign of the reactor to achieve a more balanced operation of the two segments.

To address this, a parametric CFD study was carried out in which several geometric parameters were varied to improve thermal uniformity and performance. Within the investigated design space, the axial length of the upper bed was identified as the most influential parameter. The study also showed that the way the incoming air is distributed between the two inlets plays a key role. Based on these findings, two modifications were selected for implementation: (i) adjusting the segment lengths to obtain nearly equal sorbent volumes and (ii) introducing a concentric inlet diffuser to split the flow more evenly.

In the baseline design, both segments had the same axial length (200 mm) to provide nominally similar flow paths. In the original design, the two bed segments were given the same axial length to provide nominally similar flow paths and energy-release potential. This choice, however, yielded an uneven sorbent distribution: the upper segment (segment 1) contains about 31.5 L of zeolite, whereas the lower segment (segment 2) contains only about 26 L. The time-averaged mass flow rates through the upper and lower inlets are 0.009 and 0.013 kg/s, respectively. Thus, the upper bed combined a larger sorbent volume with a lower mass flow, which led to a longer reaction time but a lower temperature peak, while the lower bed had less sorbent but a higher mass flow, yielding a higher peak temperature but a shorter discharge. This mismatch explains the different outlet temperatures and discharge durations observed at the two exits, as can be seen in Figure 12a.

In the improved design, a concentric inlet diffuser was added to redistribute the gas so that a larger share of the flow is directed to the upper segment. With the diffuser, the time-averaged mass flow rates were adjusted to 0.010 kg/s for the upper segment and 0.012 kg/s for the lower segment. In addition, the axial length of the upper section was reduced from 200 mm to 182 mm, while keeping the total reactor length, and thus the total reactor volume, unchanged. This adjustment led to almost equal zeolite volumes in the two beds, approximately 28.8 L in the upper segment and 28.5 L in the lower segment. Within the tested parameter range, this combination of a more balanced mass-flow split and nearly equal sorbent volumes provided the best match of outlet-temperature histories and discharge durations at the two exits. Figure 12 compares the outlet-temperature on the two sides of the reactor for the first and improved designs, (Figures 12a,b, respectively), highlighting the pronounced imbalance in the baseline configuration and its mitigation in the improved one. The corresponding velocity fields for the initial and improved geometries at 80 kg/h are shown in Figures 13a,b; the color scale is limited to 0.15 m/s to highlight the flow structure near the bed inlets.

Figures 14a,b illustrate how these geometric changes influence the temperature evolution inside the reactor for the case with *MFR* of 80 kg/h and *Pw* of 25 mbar. In the baseline configuration, one section heats up and advances faster, so the warm zone and reaction front are clearly asymmetric, and one side cools significantly earlier than the other. In the optimised design, the overall front shape is similar, but it becomes more symmetric: both segments progress at a comparable rate, outlet temperatures are closer to each other, and the warm region persists slightly longer, indicating a more balanced utilisation of the storage material.

To quantify the performance gain, a temperature threshold is introduced to capture the period of high-grade heat delivery. A useful-heat threshold is defined as:

$$T_{thr} = 0.95 T_{max}$$

Under the present conditions the achievable peak outlet temperature is around $T_{max} \approx 80$ °C, giving $T_{thr} \approx 76$ °C (dotted line) in Figure 15. The corresponding discharge time

$$t_{high} = time\ for\ which\ T_{out,avg} \geq T_{thr},$$

measures how long the system can supply heat above this level. For $\dot{m} = 80$ kg/h (Figure 15a), the initial design maintains $T_{out,avg}$ above 76 °C for $t_{high} = 4.88$ h, whereas the improved configuration does so for 5.95 h, i.e. an increase of about 22%. The arrows in Figure 15 mark the interval above the threshold, and the vertical dotted lines indicate when each curve falls below T_{thr}. Repeating the same analysis for $\dot{m} = 50$ kg/h (Figure 15b), t_{high} rises from 7.75 h for the baseline to 9.41 h for the improved design, again an enhancement of roughly 21%–22%, showing that the geometric optimisation is effective across different mass flow rates.

In terms of energy, the useful heat from the reactor increases from 8.25 kWh in the initial design (with about 0.45 kWh of losses) to 8.49 kWh in the optimised configuration (losses ≈0.51 kWh). For the given reactor volume, this corresponds to an increase in energy density from approximately 143.3 kWh/m^3 to 147.65 kWh/m^3.

7 Conclusion

This work presents a detailed CFD investigation of a segmented open sorption heat-storage reactor filled with zeolite 13XBF. The reactor delivers useful energy outputs between about 24 and 30 MJ, while maintaining a low static pressure drop of approximately 71–203 Pa over mass-flow rates from 50 to 120 kg/h. The variation in energy output is governed mainly by the humidity of the inlet air: increasing the water-vapor partial pressure P_w from 5 to 25 mbar raises the useful energy by about 24% and the energy density from 115.6 to 143.3 kWh/m^3 (≈+24%), For a zeolite volume of 57.5 L. Lowering the initial and inlet air temperature from 50 °C to 20 °C at constant P_w further increases the temperature lift and useful energy. Variations in air mass flow rate primarily affect thermal power and discharge duration: higher flow rates increase instantaneous power and peak outlet temperature, but only slightly change the total useful energy and shorten the time during which the outlet temperature remains near or above the target level. This establishes a clear operational trade-off between power output, temperature quality and autonomy, indicating that the flow rate must be coordinated with inlet humidity and temperature to achieve desired outlet conditions.

The validated CFD model was also used as a design tool to diagnose and mitigate performance losses caused by non-uniform sorption-front propagation and outlet imbalance between the two segments. In the baseline geometry, both segments have the same axial length, but the upper bed contains more zeolite (31.5 vs. 26 L) and receives less air (0.009 vs. 0.0126 kg/s). Consequently, the lower segment reaches a higher peak outlet temperature, while the upper segment exhibits a longer discharge period due to the combination of larger sorbent mass and lower mass flow. This uneven utilisation results in different outlet temperatures and discharge durations at the two exits. A simulation-driven parametric study identified segment length and inlet flow distribution as key design variables. In the improved configuration, a concentric inlet diffuser redistributes the gas, adjusting the time-averaged mass flows to about 0.010 and 0.012 kg/s in the upper and lower segments, respectively. In parallel, the axial length of the upper bed was reduced from 200 mm to 182 mm while keeping the total reactor length, and thus the total volume, unchanged. This yields nearly equal zeolite volumes of 28.8 and 28.5 L in the two segments. The redesigned reactor exhibits more similar outlet-temperature histories and discharge durations at both exits and a more symmetric propagation of the thermal and sorption fronts. For a mass flow rate of 80 kg/h, the high-grade discharge time (defined by T_{thr} = 76 °C) increases from 4.88 h to 5.95 h (≈+22%), while the volumetric energy density rises from about 143.3 to 147.6 kWh/m^3 (≈+3%). These results demonstrate that targeted geometric optimization of flow distribution and segment sizing can significantly enhance the performance of segmented open sorption reactors and underline the value of CFD-based design methodologies for future sorption heat-storage systems.

8 Outlook and future work

The current study demonstrates the capability of CFD-based analysis to reveal key operational and design sensitivities in open

sorption heat storage systems. Building on these insights, the model will be extended to simulate the charging (desorption) process to assess complete storage-cycle efficiency. Beyond the design refinement achieved in this work, future research will pursue a multi-objective optimization of reactor geometry and operating parameters to identify optimal trade-offs among efficiency, power density, and material utilization. Future work can also focus on conducting experiments on the optimized reactor concept.

Data availability statement

The raw data supporting the conclusions of this article will be made available by the authors, without undue reservation.

Author contributions

EA: Validation, Methodology, Visualization, Conceptualization, Formal Analysis, Data curation, Investigation, Software, Writing – original draft. DT: Writing – review and editing, Conceptualization, Methodology, Investigation. GF: Project administration, Writing – review and editing, Conceptualization, Supervision.

Funding

The author(s) declared that financial support was received for this work and/or its publication. The work was financially supported by the Saarland Ministry of Finance and for Science in the project EnFoSaar.

Conflict of interest

The author(s) declared that this work was conducted in the absence of any commercial or financial relationships that could be construed as a potential conflict of interest.

Generative AI statement

The author(s) declared that generative AI was not used in the creation of this manuscript.

Any alternative text (alt text) provided alongside figures in this article has been generated by Frontiers with the support of artificial intelligence and reasonable efforts have been made to ensure accuracy, including review by the authors wherever possible. If you identify any issues, please contact us.

Publisher's note

All claims expressed in this article are solely those of the authors and do not necessarily represent those of their affiliated organizations, or those of the publisher, the editors and the reviewers. Any product that may be evaluated in this article, or claim that may be made by its manufacturer, is not guaranteed or endorsed by the publisher.

References

Abohamzeh, E., and Frey, G. (2022). Numerical investigation of the adsorption process of zeolite/water in a thermochemical reactor for seasonal heat storage. *Energies* 15 (16), 5944. doi:10.3390/en15165944

Abohamzeh, E. S., Hosseinizadeh, S. E., and Frey, G. (2024). Numerical investigation and response surface optimization of a sorption heat storage system's performance using Y-shaped fins. *J. Energy Storage* 84, 110803. doi:10.1016/j.est.2024.110803

Adler, R. (2000). Stand der Simulation von heterogen-gaskatalytischen Reaktionsabläufen in Festbettrohrreaktoren—Teil 1. *Chem. Ing. Tech.* 72 (6), 555–564. doi:10.1002/1522-2640(200006)72:6<555::aid-cite555>3.0.co;2-#

Bathen, M., and Bäth, M. (2001). *Adsorptionstechnik*. Berlin and New York: Springer.

Bering, B. P., Dubinin, M., and Serpinsky, V. (1966). Theory of volume filling for vapor adsorption. *J. Colloid Interface Sci.* 21 (4), 378–393. doi:10.1016/0095-8522(66)90004-3

Cengel, Y. A., and Boles, M. A. (2002). *Thermodynamics: an engineering approach*. New York: McGraw-Hill.

Do, D. D. (1998). *Adsorption analysis: Equilibria and kinetics*. London: Imperial College Press.

Duquesne, E. P., Toutain, J., Sempey, A., Ginestet, S., and Palomo del Barrio, E. (2014). Modeling of a nonlinear thermochemical energy storage by adsorption on zeolites. *Appl. Therm. Eng.* 71, 469–480. doi:10.1016/j.applthermaleng.2014.07.002

Farisy, A. (2022). "Einsatz von offenen Adsorptionsspeichersystemen zur Langzeit- bzw,". *Saarbrücken.saisonalen Speicherung solarer Wärme Wohngebäuden. Master's thesis, htw saar – Hochschule für Tech. und Wirtschaft des Saarl.*

Fasano, A. P., Bergamasco, L., Lombardo, A., Zanini, M., Chiavazzo, E., and Asinari, P. (2019). Water/ethanol and 13X zeolite pairs for long-term thermal energy storage at ambient pressure. *Front. Energy Res.* 7, 148. doi:10.3389/fenrg.2019.00148

Gao, Y. L., Wang, S., Sun, Y., Wang, J., Hu, P., Shang, J., et al. (2023). Effect of charging operating conditions on open zeolite/water vapor sorption thermal energy storage system. *Renew. Energy* 215, 119033. doi:10.1016/j.renene.2023.119033

Glueckauf, E. (1955). Theory of chromatography. Part 10.—Formulæ for diffusion into spheres and their application to chromatography. *Trans. Faraday Soc.* 51, 1540–1551. doi:10.1039/tf9555101540

Hahne, E., Song, Y. M., and Gross, U. (1991). "Measurements of thermal conductivity in porous media," in *Convective heat and mass transfer in porous media* (Dordrecht: Springer Netherlands), 849–865.

Hassanabadi, S., Girnik, I. S., Ebadi, M., and Bahrami, M. (2025). A novel sorption reactor for sorption heat transformers: thermal energy storage system. *Energy Convers. Manag.* 328, 119618. doi:10.1016/j.enconman.2025.119618

Hu, G. S., Wang, S., Wang, J., Jiang, S., Liang, Y., Ma, Z., et al. (2022). Thermal performance analysis of the sorption heat storage system with packed bed based on a spatially resolved 2D model. *Sustain. Energy Technol. Assessments* 49, 101. doi:10.1016/j.seta.2021.101753

Jänchen, R. H., Herzog, T. H., Gleichmann, K., Unger, B., Brandt, A., Fischer, G., et al. (2015). Performance of an open thermal adsorption storage system with Linde type A zeolites beads versus honeycombs. *Microporous Mesoporous Mater.* 207, 179–184. doi:10.1016/j.micromeso.2015.01.018

Kast, W. (1988). *Adsorption aus der Gasphase. Ingenieurwissenschaftliche Grundlagen und technische Verfahren*. Weinheim: Verlag Chemie.

Kerskes, H., Mette, B., Bertsch, F., Asenbeck, S., and Drück, H. (2011). "Development of a thermo-chemical energy storage for solar thermal applications," in *Proceedings of the ISES Solar World Congress*.

Kerskes, H., Bertsch, F., Asenbeck, S., Mette, B., and Drück, H. (2012). "Abschlussbericht CWS – Chemische Wärmespeicherung mittels reversibler Feststoff-Gasreaktionen," in *Teilvorhaben Niedertemperatur-Wärmespeicherung*.

Krese, U., Baldvinsson, G., Soldo, B., and Stritih, U. (2018). Thermochemical seasonal solar energy storage for heating and cooling of buildings. *Energy Build.* 164, 239–253. doi:10.1016/j.enbuild.2017.12.057

Kuznik, F., Gondre, D., Johannes, K., Obrecht, C., and David, D. (2019). Numerical modelling and investigations on a full-scale zeolite 13X open heat storage for buildings. *Renew. Energy* 132, 761–772. doi:10.1016/j.renene.2018.07.118

Kwasi-Effah, C. C., and Okpako, O. (2025). Comprehensive review of emerging trends in thermal energy storage mechanisms, materials and applications. *Front. Energy Res.* 13, 1651471. doi:10.3389/fenrg.2025.1651471

Lagergren, S. (1898). *About the theory of so-called adsorption of soluble substances. Kungliga Svenska Vetenskapsakademiens Handlingar*, 24, 1–39.

Mersmann, A. M., and Kind, M. (1980). *Thermische Verfahrenstechnik: grundlagen und Methoden*. Berlin and Heidelberg: Springer.

Mette, B. (2014b). *Experimentelle und numerische Untersuchungen zur Reaktionsführung thermochemischer Energiespeicher*. Stuttgart: Universität Stuttgart. PhD thesis.

Mette, B., Kerskes, H., and Drück, H. (2014a). Experimental and numerical investigations of different reactor concepts for thermochemical energy storage. *Energy Procedia* 57, 2380–2389. doi:10.1016/j.egypro.2014.10.246

Padamurthy, R. P., Nandanavanam, J. A., and Rajagopalan, P. (2022). Sustainable and open sorption system for low-temperature heat storage applications. *Int. J. Energy Res.* 46 (14), 20004–20020. doi:10.1002/er.7867

Palacios, A. M., Navarro, M. E., Barreneche, C., and Ding, Y. (2022). Water sorption-based thermochemical storage materials: a review from material candidates to manufacturing routes. *Front. Therm. Eng.* 2, 1003863. doi:10.3389/fther.2022.1003863

Qian, Y., Han, Z., Zhan, J. H., Liu, X., and Xu, G. (2018). Comparative evaluation of heat conduction and radiation models for CFD simulation of heat transfer in packed beds. *Int. J. Heat Mass Transf.* 127, 573–584. doi:10.1016/j.ijheatmasstransfer.2018.06.127

Qiu, H. L., Lv, L., Pan, B. C., Zhang, Q. J., Zhang, W. M., and Zhang, Q. X. (2009). Critical review in adsorption kinetic models. *J. Zhejiang Univ. – Sci. A* 10 (5), 716–724. doi:10.1631/jzus.a0820524

Reichl, P. M., Lager, D., Englmair, G., Zettl, B., and Popovac, M. (2016). Fluid dynamics simulations for an open-sorption heat storage drum reactor based on thermophysical kinetics and experimental observations. *Appl. Therm. Eng.* 107, 994–1007. doi:10.1016/j.applthermaleng.2016.06.119

Schmidt, M., and Linder, M. (2020). A novel thermochemical long term storage concept: balance of renewable electricity and heat demand in buildings. *Front. Energy Res.* 8, 137. doi:10.3389/fenrg.2020.00137

Seidel, H. (1965). Untersuchungen zum Wärmetransport in Füllkörpersäulen. *Chem. Ing. Tech.* 37 (11), 1125–1132. doi:10.1002/cite.330371108

Sircar, S., and Hufton, J. (2000). Why does the linear driving force model for adsorption kinetics work? *Adsorption* 6, 137–147. doi:10.1023/a:1008965317983

Strong, C. C., Carrier, Y., and Handan Tezel, F. (2022). Experimental optimization of operating conditions for an open bulk-scale silica gel/water vapour adsorption energy storage system. *Appl. Energy* 312, 118533. doi:10.1016/j.apenergy.2022.118533

Tenny, K., and Cooper, J. (2017). "Ideal gas behavior," in *StatPearls.* (Treasure Island (FL): StatPearls Publishing).

Tsotsas, E. (2002). "Wärmeleitung und Dispersion in durchströmten Schüttungen," in *VDI-Wärmeatlas* (Berlin).

Weber, R., Asenbeck, S., Kerskes, H., and Jaudas, R. (2016). *Abschlussbericht für das Projekt SolSpaces: Entwicklung und Erprobung einer autarken solaren Wärmeversorgung für energieeffiziente Kompaktgebäude*. Stuttgart: Universität Stuttgart, Institut für Thermodynamik und Wärmetechnik (ITW).

Winterberg, M. T., Tsotsas, E., Krischke, A., and Vortmeyer, D. (2000). A simple and coherent set of coefficients for modelling of heat and mass transport with and without chemical reaction in tubes filled with spheres. *Chem. Eng. Sci.* 55 (5), 967–979. doi:10.1016/s0009-2509(99)00379-6

Zehner, P., and Schlünder, E. U. (1970). Wärmeleitfähigkeit von Schüttungen bei mäßigen Temperaturen. *Chem. Ing. Tech.* 42 (14), 933–941. doi:10.1002/cite.330421408

Nomenclature

A	Adsorption potential J/mol
A_{ht}	Heat-transfer area m^2
B	Shape parameter in the Zehner–Schlünder model for spherical particles
$c_{p,a}$	Specific heat of dry air J/(kg K)
$c_{p,s}$	Specific heat of steel J/(kg K)
$c_{p,z}$	Specific heat of zeolite-13XBF J/(kg K)
d_1	The diameter of the air channel mm
d_m	Macropore diameter nm
d_p	Zeolite particle diameter mm
$d_{in,pipe}$	Inlet-pipe diameter mm
d_1	Reactor outer diameter mm
D_{ax}	Axial dispersion coefficient m^2/s
D_{eff}	Effective diffusion coefficient (LDF model) m^2/s
D_{ges}	Overall diffusion coefficient m^2/s
D_{Kn}	Knudsen diffusion coefficient m^2/s
D_r	Radial dispersion coefficient m^2/s
E_{DA}	Characteristic adsorption energy (Dubinin–Astakhov model) kJ/kg
ESD	Energy-storage density kWh/m^3
h_{amb}	Convective heat-transfer coefficients $W/(m^2\ K)$
h_1, h_2	Heights of upper and lower segments mm
i	Index of data point (from one to N)
k_{ins}, k_m	Thermal conductivity of insulation/metal wall W/(m K)
k_s	Conductivity ratio of solid to fluid
k_{ss}	Thermal conductivity of stainless steel W/(m K)
$K_{1,h}$	Constant for effective thermal conductivity
$K_{2,h}$	Constant for effective thermal conductivity
K_{ax}	Effective axial thermal conductivity W/(m K)
k_c	Dimensionless factor in the Zehner–Schlünder correlation.
K_r	Effective radial thermal conductivity W/(m K)
h	Total length of the reactor module mm
M_a	Molar mass of air g/mol
M_w	Molar mass of water vapor g/mol
MAE	Mean absolute error
$MAPE$	Mean absolute percentage error
MFR	Mass-flow rate of air kg/h
n	Exponent in Dubinin–Astakhov equation –
N	Total number of data points used in the comparison
$NRMSE$	Normalized root mean square error
p_s	Saturation vapor pressure Pa
p_w	Partial pressure of water vapor Pa
Q_{amb}	Heat exchange with ambient W
R	Universal gas constant J/(mol K)
R_1, R_2, R_3	Inner/outer wall radii (with insulation) m
R_a	Specific gas constant of dry air J/(kg K)
$RMSE$	Root mean square error
R_{tot}	Total thermal resistance K/W
Rw	Specific gas constant of water vapor J/(kg K)
r	Radial coordinate m
r_c	Curve radius mm
t	Wall/channel thickness mm
T	Temperature K
T_{amb}	Ambient temperature K
T_{in}	Inlet temperature K
$T_{exp,i}$	Experimental temperature at data point i
$T_{sim,i}$	Simulated temperature at data point i
μ	Tortuosity –
U	Overall heat-transfer coefficient W/(m K)
u_0	Superficial velocity m/s
W^*	Equilibrium volumetric uptake mL/kg
$W_{0,DA}$	Maximum adsorption volume mL/kg
X, X^*	Instantaneous/equilibrium mass loading $kg_{water}/kg_{zeolite}$
$X_{init,ads}$	Initial adsorbed loading $kg_{water}/kg_{zeolite}$
z	Axial coordinate m
α	Angle of the bed inlet Deg
β	Angle of the bed outlet Deg
$\beta_{20\,℃}$	Thermal expansion coefficient of adsorbate at 20 ℃ K^{-1}
ε_b	Bed porosity –
ε_p	Particle porosity –
μ_a	Dynamic viscosity of air Pa s
λ_a	Thermal conductivity of air
λ_z	Thermal conductivity of zeolite-13XBF W/(m K)
φ	Degree of pore filling –
$\rho(T)$	Density of adsorbed water kg/m^3
ρ_a	Density of moist air kg/m^3
ρ_s	Density of stainless steel kg/m^3
ρ_z	Particle density of zeolite kg/m^3
$\rho_{z,b}$	Bulk density of zeolite kg/m^3
$\Delta h_{ads,m}$	mean (average) specific adsorption enthalpy kJ/kg

Subscripts and superscripts

a	Air (dry)
ads	Adsorption
amb	Ambient
ax	Axial
b	Bulk
in	Inlet
out	Outlet
r	Radial
s	Steel
w	Water vapor
z	Zeolite/solid
*	Equilibrium condition